Modelling Wave-Particle Interactions with high-m Guided Poloidal Waves

by

Guy Whittall-Scherfee

A thesis submitted in partial fulfillment of the requirements for the degree of

Master of Science

Department of Physics

University of Alberta

©Guy Whittall-Scherfee, 2020

Abstract

The development of accurate models of drift resonance between H^+ ions and Alfvénic ultra-low frequency (ULF) waves is crucial for understanding particle dynamics in the Earth's inner magnetosphere. However, full solutions to the wave equations are complex and approximations are required to derive numerical solutions. This thesis investigates the results obtained from one such approximation, focusing on the poloidal components of the wave, and reviews previously published results using the same assumption. These results are recreated and disagreements between the published results and the recreation are discussed. We use a full Lorentz particle integrator for test particle motion along with our analytic solutions to the field equations to analyze wave-particle resonance and the variation in particle invariants. We conclude that the poloidal mode approximation can lead to unrealistic magnetic fields aligned with the Earth's magnetic field, and in some cases, these fields can violate Faraday's Law.

Preface

This thesis is an original work by Guy Whittall-Scherfee.

Chapter 4 of this thesis follows the derivation of poloidal field components as outlined by Chengrui Wang in his 2018 thesis, ”Numerical Modeling of Drift Resonance and Drift-bounce Resonance between Ultra-low Frequency Waves and Energetic Particles in the Inner Magnetosphere”. Both works are based on Rankin 2014.

Chapter 5 includes comparisons to the results reported in C. Wang, Rankin, and Zong 2015 and C. Wang, Rankin, Y. Wang, et al. 2018. The recreation of the fields was completed using fields left by the author for the explicit purpose of recreating their results.

Dedication

To Austin, Madison and my Mother

To my Father, "A soul in tension that's learning to fly"

Acknowledgements

I would like to thank Dr. Richard Sydora for his flexibility and guidance in the writing of this thesis and Dr. Robert Rankin for the pivotal role he played in guiding the research contained in this thesis. I would also like to acknowledge the support Dr. Craig Heinke provided as the graduate chair. A special thanks to Alex Degeling who offered insight and a valued second pair of eyes in my derivations and modeling.

Thank you to my colleagues and friends that listened to my mad ramblings and provided help throughout my program. Charles Jensen, Leon Olifer, Mason Protter, and Pramodh Yapa all provided comfort and insight in different ways that made this work possible.

Finally, I would like to thank the four people closest to me. Thank you Mom, for your constant love and support. You have always been there for me. Thank you Austin for your continual friendship. You helped me feel at home, even when I was thousands of miles away. Thank you Madison for your love and patience. Your encouragement and love guided me out of the dark. Thank you Dad for everything you gave me. I hope you are at rest.

Contents

List of Figures

List of Tables

Chapter 1

Introduction

The primary objective of space physics research is to develop a comprehensive understanding of the physics behind space weather. While this encompasses research from the solar cycle and heliophysics down to Earth's natural magnetic field. The focus of this thesis will rest on the interaction between waves and particles in the near-Earth environment. This introduction will help frame this work within the larger scope of space physics, starting with the sun and solar wind. We will then discuss the relevant areas of the magnetosphere and end with an overview of geomagnetic storms and a brief summary of Ultra Low Frequency (ULF) waves.

1.1 The Solar Wind

The pressure differential between the hot solar corona and interplanetary space drives plasma away from the Sun. This hot plasma is highly conductive and remains "frozen" to the Sun's magnetic field lines as they are forced out through

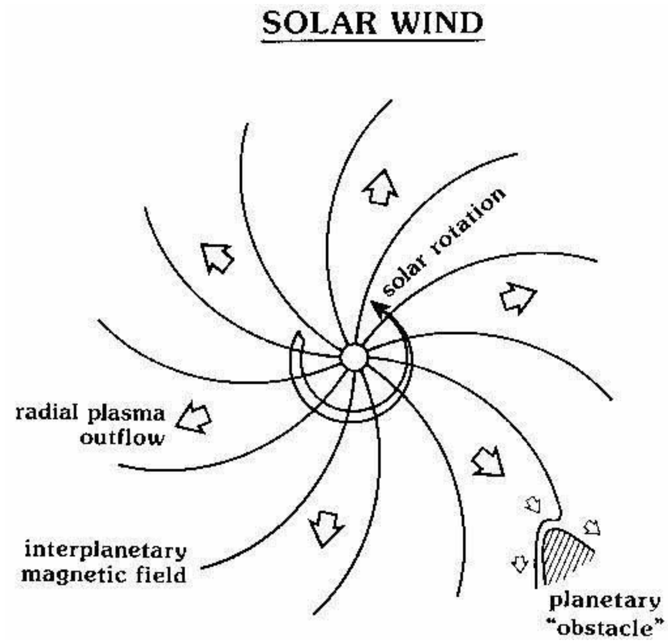

Figure 1.1: Interplanetary magnetic field lines curved due to the rotation of the Sun while plasma flows radially outward (Allan and Poulter 1992).

space due to the solar wind. As the sun's magnetic field is carried out into the heliosphere it forms the interplanetary magnetic field (IMF). Despite it's radial propagation the rotation of the sun causes the field to become curved as shown in Figure 1.1. This curvature is know as the Parker-Spiral, named after Eugene Parker, the first man to postulate the existence of the solar wind in 1958.

This spiral is also impacted by variation in the Sun's magnetic field. If we model the Sun's magnetic field as a dipole perpendicular to the planetary plane, the radial flow of the solar wind at the equator will stretch out the magnetic field lines away from the Sun. These anti-parallel, magnetic field lines produce a current sheet between them in the equatorial plane, known as the heliospheric current sheet. However, the Sun's rotational axis and its magnetic axis are not perfectly perpendicular to the equatorial plane. This results in oscillations in the

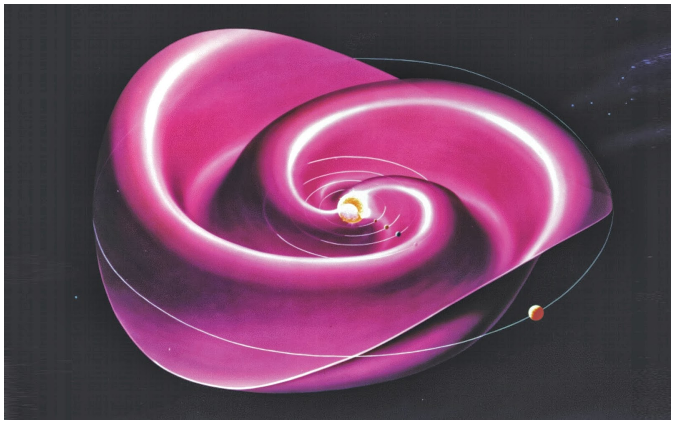

Figure 1.2: Interplanetary magnetic field lines curved due to the rotation of the Sun while plasma flows radially outward (Werner 1980).

current sheet formation that resemble a ballerina skirt, as seen in Figure 1.2

1.2 Earth's Magnetic Structure

Similar to the Sun, the Earth generates its own magnetic field. This field can be modeled as a simple dipole which decreases radially as r^3. Further from the Earth, the field begins to be distorted by the impact of the solar wind, compressing the Sun-ward side and stretching the night side region out past the moon. The interaction between these two fields generates a variety of complex structures, summarized in Figure 1.3. This section will focus on the bow shock, magnetosheath, radiation belts and the ionosphere.

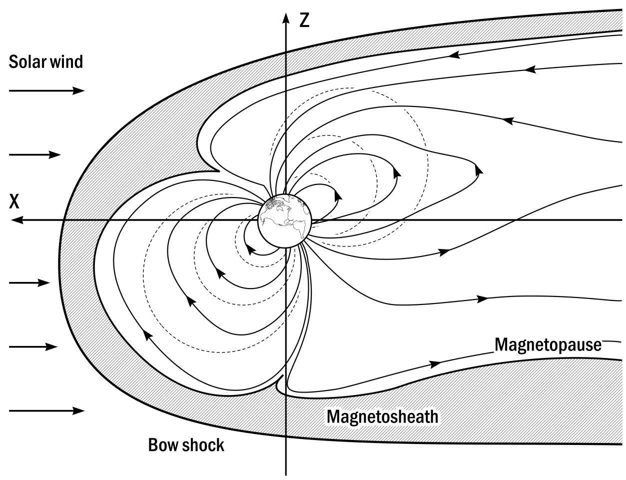

Figure 1.3: The interaction of the solar wind with the Earth's magnetic field. Key structures related to this thesis are labeled in the local magnetic environment. Dotted lines represent the Earth's unperturbed dipole field lines. The solid lines represent the Earth's magnetic field lines while interacting with the Solar wind. Image credit to Andy Kale

1.2.1 The Bow Shock and the Magnetosheath

As the solar wind streams towards the Earth it will impact the Earth's magnetic field. The boundary between the two fields is called the bow shock. The solar wind travels at super sonic speeds and when it impacts the Earth's field it results in a shock. The disruption of the plasma by this barrier converts some of the velocity of the particles traveling in the solar wind to thermal energy. This increase in temperature creates a highly turbulent region directly Earth-side of the bow shock, called the magnetosheath. The dynamics involved with shocks are complex and a discussion is best left to Kivelson and Russell 1995.

The magnetopause is the barrier between the solar wind and the Earth's magnetic field. This region is located around ten Earth radii away at the sub-point, though the exact distance varies depending on the ram pressure of the solar wind. The plasma can then travel around the Earth's magnetic field like water around the bow of a boat. The magnetopause is the boundary between solar and terrestrial magnetic fields and is defined as the last closed magnetic field line from the Earth.

The Dungey cycle is a widely accepted theory in near Earth plasma dynamics. It states that the interactions between the solar wind and terrestrial magnetic field drives the dynamics of the magnetosphere (J. W. Dungey 1961; J. W. Dungey 1965). The primary mechanism by which magnetic flux can be transferred is magnetic reconnection in the day side magnetopause and magnetotail. Magnetic reconnection occurs when two magnetic domains splice together, redirecting magnetic flux. The Dungey cycle is depicted in Figure 1.4

Line 1 in Figure 1.4 marks the starting point of magnetic reconnection. The newly spliced magnetic field lines are pulled back as far as 1000 earth radii, as depicted by field lines 2-5. The motion of the anchor of these field lines is depicted in the lower image of Figure 1.4. These fields end up in the nightside region of the

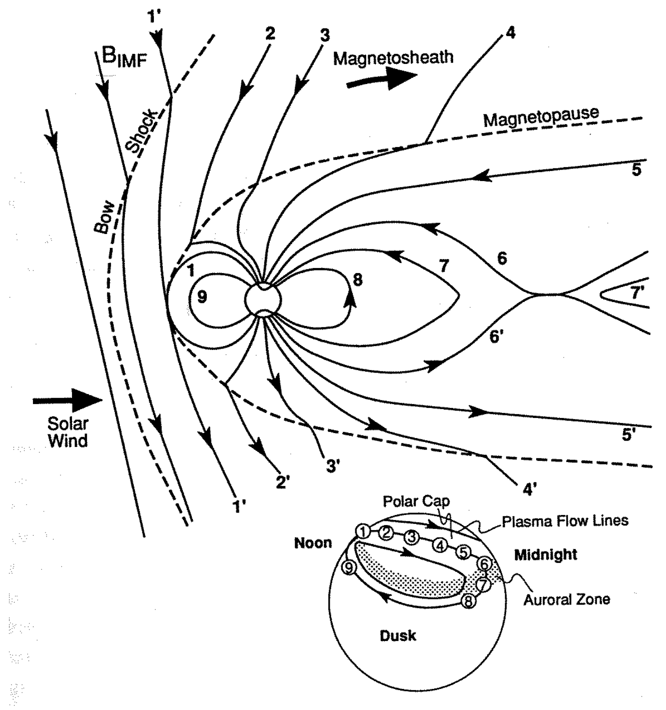

Figure 1.4: Over view of magnetospheric convection. 1) The Southward IMF hits the Earth's magnetic field, leading to dayside reconnection. 2-5) The IMF pulls the magnetic field lines over the poles towards the magneotail. 6) Magnetic reconnection occurs in the magnetotail. 7-8) The magnetic field is brought back towards the Earth. 9) The field line returns to the dayside to repeat the cycle. The motion of the fields lines at the poles is outlined in the bottom figure (Kivelson and Russell 1995).

Earth's magnetic field which is referred to as the magnetotail. Due to the dipole nature of the Earth's magnetic field, there are two lobes that form in the northern and southern region of the tail. Similar to the heliospheric current sheet, these two regions of oppositely direction magnetic field create a dawn to dusk current called the tail current sheet.

After the open field lines reconnect (field line 6 in Figure 1.4), magnetic tension will cause the newly closed field lines to return to the Earth. During this process, the field lines will rotate around the Earth returning to the dayside (9), where the cycle can begin again. This discussion has focused on the motion of the field lines but it is important to recall that the plasma is still fixed to these fields. This is due to the high conductivity of the plasma which can be considered an infinitely conductive fluid. As these particles move around the Earth the changes in magnetic and electric fields will cause a variety of current systems to develop, most notably for this thesis is the ring current. A full discussion of these dynamics can be found in Section 2.2.

It is common when discussing the Earth's magnetic field lines to talk about distance in terms of L-shells. L-shells are used to label magnetic field lines by measuring the equatorial crossing point of the field line from the Earth. For example, most of the work done in this thesis is focused around L-shell value of 5.7, which corresponds to the magnetic field lines that are 5.7 Earth radii away from the center of the Earth in the equatorial plane. We will be shortening L-shell to L for this thesis.

1.2.2 The Radiation Belts

The radiation belts are a two band, toroidal structure of high energy charged particles. They are also referred to as the Van Allen belts, after James Van Allen who discovered them in 1959 (Van Allen, McIlwain, and Ludwig 1958). This structure is a general formation that has been found around many planets with a sufficiently strong magnetic field including; Mercury, Jupiter, Saturn, Uranus and Neptune. The Earth's inner belts result from charged particle interactions with the planets magnetic field (Barth, Dyer, and Stassinopoulos 2003; Kivelson and Bagenal 2014). The inner belt extends from around 1000km above the Earth to L = 2, though the inner boundary can change due to variations in the ionosphere. The outer belt extends from L = 3-6, with a slot region between theses two belts.

The inner radiation belt is home to protons with energies in the tens of MeV range, and electrons with energies in the range of 100 keV, which orbit the Earth. The main source of these high energy particles comes from the decay of neutrons resulting from cosmic ray interactions with the ionosphere (Kivelson and Russell 1995). The outer radiation belt is made up primarily of very high energy electrons in the MeV range as well as high energy ions. For example, oxygen and some hydrogen ions have been found in this region in the 200-350 keV range (Oimatsu, Nosé, Teramoto, et al. 2018; Oimatsu, Nosé, K. Takahashi, et al. 2018).

There are also times when there is a separation of the outer belt into two separate belts. This forms a three belt structure that has recently been observed from the Van Allen Probes. This new region is much more reactive to solar storms with a 2013 observation lasting for only four weeks before an increase in the solar wind wiped it out (Thorne et al. 2013). The three belts, as well as the slot region can be seen in Figure 1.5.

1.3 Ionosphere

The ionosphere is the closest region to the Earth that we will be studying in this thesis. In the ionosphere, the Earth's magnetic field lines are the most dense and

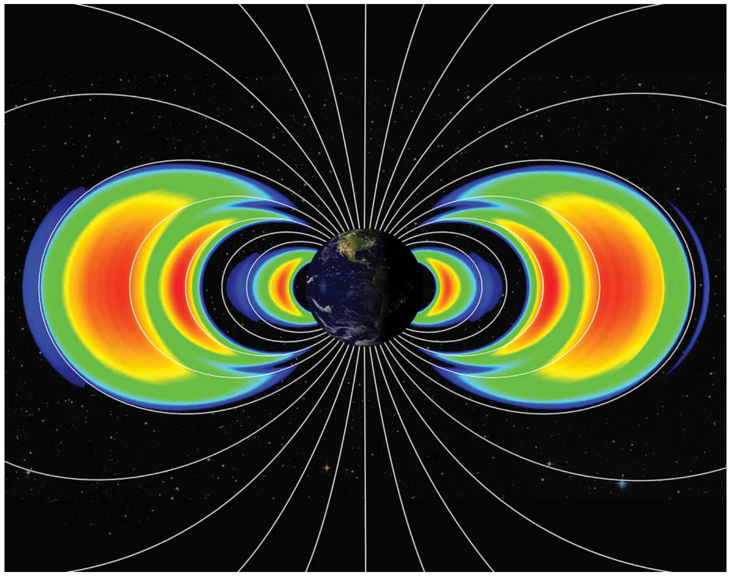

Figure 1.5: Depiction of the three radiation belts. Credit to NASA's Goddard Space Flight Center/Johns Hopkins University, Applied Physics Laboratory

the impact of the ionosphere on particle dynamics is most apparent. The most obvious interactions between space weather and the ionosphere are the aurora which may result from particle acceleration. The ionosphere is the primary sink and tether for the field lines and for the purpose of this thesis we will assume that the ionosphere has infinite conductivity and that the magnetic field lines are fixed at the ionosphere.

1.4 Geomagnetic Activity

We have hinted at variations in the interaction between the solar wind and the Earth's magnetic field. Here, we will discuss the connections between the two in more depth. There are two categories of large scale events that impact the Earth's magnetic field, geomagnetic storms and substorms.

1.4.1 Geomagnetic storms

Geomagnetic storms result from increased coupling between the solar wind and the magnetosphere, resulting in increased energy transfer. Coronal mass ejections and similar solar eruptive events increase the dynamic pressure of the solar wind which compresses and transfers energy into the magnetosphere. Here the energy increases the intensity of the ring current. The ring current is an electric current that is carried by ions and electrons that drift in opposite directions around the Earth. These storms can be divided into three parts, the initial phase, the main phase and the recovery phase.

The initial phase is noted by an increase in disturbance storm time (Dst), a measurement of the change in the Earth's magnetic field. This increase can last between several minutes to several hours. The main phase is classified as a period of rapid and sometimes drastic decrease in Dst as drifting particles in the ring current move closer to the Earth as their energy increases. The main phase normally lasts for only a few hours but last for days. The recovery phase occurs over a period of 1-5 days as ions are lost to the solar wind and to charge exchange with neutral hydrogen and the ring current decays. This results in a gradual reduction in Dst to pre-storm levels. An example of a solar storm's impact on Dst is shown in Figure 1.6.

1.4.2 Substorms

As discussed previously in Section 1.2.1, southward IMF can couple to the Earth's magnetic field lines and transfer energy to the magnetotail by a process known

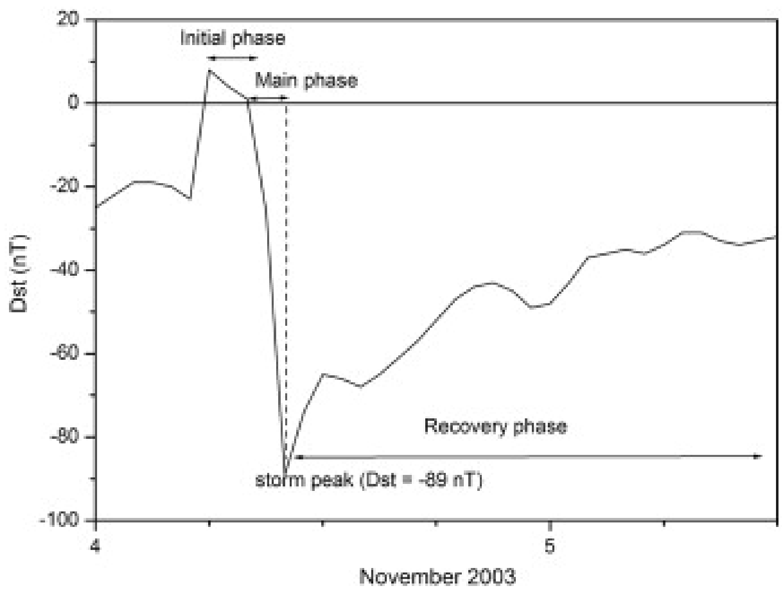

Figure 1.6: Variation in Dst index during a storm between November 4-5, 2003. The initial, main and recovery phase are labeled as well as the minimum Dst (Echer, Gonzalez, and Tsurutani 2011).

as magnetic reconnection. Following point 6 in Figure 1.4 the energy released from the reconnection region in the tail will head Earthward. The Earthward moving plasma injects energetic particles, causing the nightside magnetic field to di-polarise. This causes brightening and dynamics in the nightside aurora in the form of bright northern (aurora borealis) and southern lights (aurora australis).

Like the geomagnetic storms, substorms have three different phases. The first phase is the growth phase which is tied to an increase in the size of the polar cap as well as an increase in energy stored in the magnetotail. This energy is released during the expansion phase which is then followed by a recovery phase. The expansion phase is tied to enhancement and dynaimcs in the visible aurora.

On Earth, this activity is the main cause of different types of aurora. The two primary types are discrete and diffuse aurora. Discrete aurora are caused by electron acceleration along field lines and tends to have a more defined profile. This is the type of aurora that most people think of when they hear the term. Diffuse aurora are found on the edges of the auroral oval, towards the equator. They tend to result from lower energy electrons that pitch angle scatter as the electrons interact with plasma waves. A more complete discussion of the difference between diffuse and discrete aurora can be found in Akasofu 1974.

1.5 ULF Waves

Ultra Low frequency (ULF) waves are electro-magnetic waves with frequencies between 1mHz and 1Hz that appear in the magnetosphere and may result from internal effects like plasma instabilities, and external effects like solar wind disturbances. The first observed recording of these waves was at the Kew Observatory in 1861 (Balfour 1860).

Over the next century, the theory surrounding these observations slowly developed. The study of these waves was limited to ground observations and the research was restricted largely to taxonomy. The International Association of Geomagnetism and Aeronomy created a modern system for classification based on the period of the waves and whether it was continuous or impulse driven (Walker 2005).

Label	Frequency range (mHz)
Pc1	5000 - 200
Pc2	200 - 100
Pc3	100 - 22
Pc4	22 - 7
Pc5	7 - 2
Pi1	5000 - 22
Pi2	22 - 7

Table 1.1: International Association of Geomagnetism and Aeronomy classification of pulsations (Walker 2005)

The source of ULF waves is an active area of research in space plasma research. These sources include, Kelvin-Helmoholtz (K-H) instabilities on the magneotpause, solar wind dynamic pressure pulses, ion cyclotron resonance, and substorm particle injections (Hudson et al. 2004; Claudepierre, Elkington, and Wiltberger 2008; Fairfield et al. 2000; Hasegawa et al. 2004; Rae et al. 2005; C. Wang, Rankin, and Zong 2015; C. Wang, Rankin, Y. Wang, et al. 2018). Different sources are tied to different frequency ranges and whether the wave is continuous or impulse driven. A mathematical description of these waves will be given late in Chapter 3.

1.6 Thesis Outline

The primary objective of this thesis is to study the validity of certain assumptions in modeling drift-resonance between ULF waves and energetic ions in the inner magnetosphere. Chapter 2 provides an overview of single-particle motion in the near-earth environment. Chapter 3 discusses the magnetohydrodynamic wave model and the coupling between these waves and the particles through drift and drift-bounce resonance. Chapter 4 focuses on the derivation of analytic solutions for the poloidal mode wave model. We also compare our field equations with other simulations and discuss the validity of a poloidal mode model. The particle dynamics are covered in Chapter 5. An outline of the benchmarking used in our model as well results for simplified fields are shown. We end with a study of the particle trajectories that result from the fields in Chapter 4 and compare with recently published results.

Chapter 2

Single Particle Motion

Despite the initial complexity that the term suggest, we can begin studying plasma physics using the same equations taught in introductory physics courses. Doing so requires an important series of assumptions. The main assumption is that the charged particles, and the fields they produced, have a negligible impact compared to the external electric and magnetic fields. This allows us to study plasma behavior by focusing on single particle trajectories rather than working with the entire plasma system.

2.1 Charged Particle Dynamics

The Lorentz force describes the motion of a charged particle in a magnetic field while the Coulomb force describes the force resulting from a charged particle in an electrostatic field. These two effects can be combined into a single equation,

$$m\frac{d\mathbf{v}}{dt} = q(\mathbf{E} + \mathbf{v} \times \mathbf{B}) \tag{2.1}$$

where m is the mass of the particle, v is the particles velocity, q is the charge of the particle, E is the electric field and B is the magetic field.

For now, we will ignore the electric field. The solution to Equation 2.1, assuming a constant magnetic field, is uniform gyromotion around the magnetic field with a frequency ω_g, called the gyrofrequency or the cyclotron frequency (Baumjohann and Treumann 1997). This frequency is defined as,

$$\omega_g = \frac{qB}{m} \tag{2.2}$$

which is charge and mass dependent. Not only will electrons and ions orbit in opposite directions around this field, they will also orbit at different speeds with electrons orbiting faster than ions. r_g is the gyroradius associated with this motion and is defined as,

$$r_g = \frac{mv_\perp}{qB} \tag{2.3}$$

with $v_\perp$ defined as the velocity component perpendicular to the magnetic field.

One important property of a charged particle that is of particular interest in space physics is the pitch angle, α, which is defined as

$$\tan(\alpha) = \frac{v_\perp}{v_\parallel} \tag{2.4}$$

where $v_\perp$ is the velocity perpendicular to the magnetic field and $v_\parallel$ is the velocity along the field.

2.2 Particle Drifts

The equations previously derived have assumed a constant magnetic field and have not taken into account the effects of electric fields. The resulting drift-motion from the interaction between the magnetic and electric fields depends on the time and spatial variation of the electric and magnetic fields.

2.2.1 $E \times B$ Drift

The simplest form of drift motion is caused by isolated electric fields. We begin by introducing two new terms, the plasma current density $\mathbf{J}$, and the conductivity of the plasma, σ which are related by,

$$\mathbf{J} = \sigma(\mathbf{E} + \mathbf{v} \times \mathbf{B}) \tag{2.5}$$

In a plasma, electrons are much more mobile than protons and will react quickly to electric fields, cancelling their effects within the plasma. This means that we can treat the conductivity as infinite in most cases. This simplifies Equation 2.5 to,

$$\mathbf{E} = -\mathbf{v} \times \mathbf{B} \tag{2.6}$$

Solving for $\mathbf{v}$ leads to the generalized $\mathbf{E} \times \mathbf{B}$ drift equation

$$\mathbf{v}_{E\times B} = \frac{\mathbf{E} \times \mathbf{B}}{B^2} \tag{2.7}$$

which is charge independent meaning that ions and electrons will drift in the same direction. Note that the variation in the magnitude of the drift velocity is proportional to one over the magnetic field.

2.2.2 Gradient-B Drift

If there is a gradient in the magnetic field the particle's gyroradius will be non-uniform as the radius narrows in the stronger field and widens in the weaker field. If the overall change in field strength over a single gyroperiod is small, we can begin by representing the magnetic field as a first order Taylor expansion and breaking the velocity up into a drift along B_0, $\mathbf{v}_\nabla$ and gyration perpendicular to B_0,$\mathbf{v}_g$, component,

$$\begin{aligned}\mathbf{B} &= \mathbf{B}_0 + (\mathbf{r} \cdot \nabla)\mathbf{B} \\ \mathbf{v} &= \mathbf{v}_g + \mathbf{v}_\nabla\end{aligned} \tag{2.8}$$

as previously shown by (Baumjohann and Treumann 1997). This distinction between gyration and drift velocity components is important for modeling. The model used in this thesis includes the gyration component and models the complete trajectory of a particles motion. However, a guiding center model averages over the gyration component and focus on the motion of the drift of the center of this gyration.

We then return to Equation 2.1 for the $E = 0$ case and this time we will ignore all gyromotion terms and assume that the magnitudes of $\mathbf{v}_g \gg \mathbf{v}_\nabla$

$$m\frac{d\mathbf{v}_\nabla}{dt} = q(\mathbf{v}_\nabla \times \mathbf{B}_0) + q(\mathbf{v}_g \times (r \cdot \nabla)\mathbf{B}_0) \tag{2.9}$$

Since we are looking at drift effects that occur over timescales that are much longer than a single gyroperiod we will average our entire equation over a gyroperiod, eliminating our drift acceleration term on the left hand side. We then cross the right hand side with $\mathbf{B}_0/B_0^2$ and find that

$$\mathbf{v}_\nabla = \frac{1}{B_0^2}(\mathbf{v}_g \times (r \cdot \nabla)\mathbf{B}_0 \times \mathbf{B}_0) \tag{2.10}$$

Assuming that the motion is harmonic we can then find that the general solution to Equation 2.10 is

$$\mathbf{v}_\nabla = \frac{mv_\perp^2}{2qB^3}(\mathbf{B} \times \nabla B) \tag{2.11}$$

This drift is a particularly important one due to the dipole nature of the Earth's magnetic field. A charged particle near the Earth tends to have its motion dictated by this drift effect.

Magnetic Curvature Drift

The dipole model of the Earth's magnetic field requires curved field lines. These curves lead to a curvature drift. Curvature drift is a special case of generalized force drift which is defined in Baumjohann and Treumann 1997 as

$$\mathbf{v}_F = \frac{1}{\omega_g}\left(\frac{\mathbf{F}}{m} \times \frac{\mathbf{B}}{B}\right) \tag{2.12}$$

Particles moving along one of these curved field lines will experience a centrifugal force related to $\mathbf{v}_{Rc}$, the radius of curvature of the field, which is given by,

$$\mathbf{F}_c = mv_\parallel^2 \frac{\mathbf{R}_c}{R_c^2} \tag{2.13}$$

This can then be substituted into Equation 2.12 to find the curvature drift velocity (Baumjohann and Treumann 1997; Roederer 1970),

$$\mathbf{v}_c = \frac{mv_\parallel^2}{qR_c^2 B^2}\mathbf{R}_c \times \mathbf{B} \tag{2.14}$$

The curved magnetic field lines are weakest at the equator and strongest at the Earth's poles where the density of magnetic field lines increases. This variation in magnetic field strength can cause particles that travel along the field lines will have it's pitch angle increase. When the pitch angle reaches 90 deg the particle reflect due to the gradient force. This point of reflection is referred to as the mirror point.

The gradient and curvature drifts play an important role in forming the ring current discussed in Chapter 1. Together, these two drifts are referred to as the gradient-curvature drift or the total magnetic drift. However, this drift can act

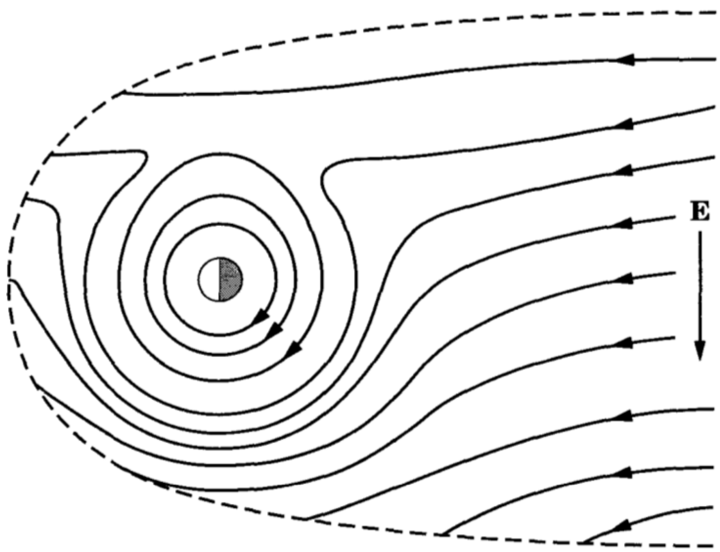

Figure 2.1: Ion particle drift motion in the equatorial plane. [Baumjohann and Treumann 1997]

in combination with the $E \times B$ drift which gives a physical description for the energization of ring current particles as show in Figure 2.1.

2.3 Adiabatic Invariants

As charged particles drift and bounce along the Earth's magnetic field, their motion can be grouped under three umbrellas; gyromotion around a field line, bounce motion between two mirror points, and drift motion around the Earth, as depicted in Figure 2.2. Each type of motion has an adiabatic invariant associated with it. Adiabatic invariants, while not always constant, can be treated as such assuming that the motion related to each invariant changes slowly over its associated time scale. As long as changes in time and space relative to the motion of the particle are small, each invariant will hold.

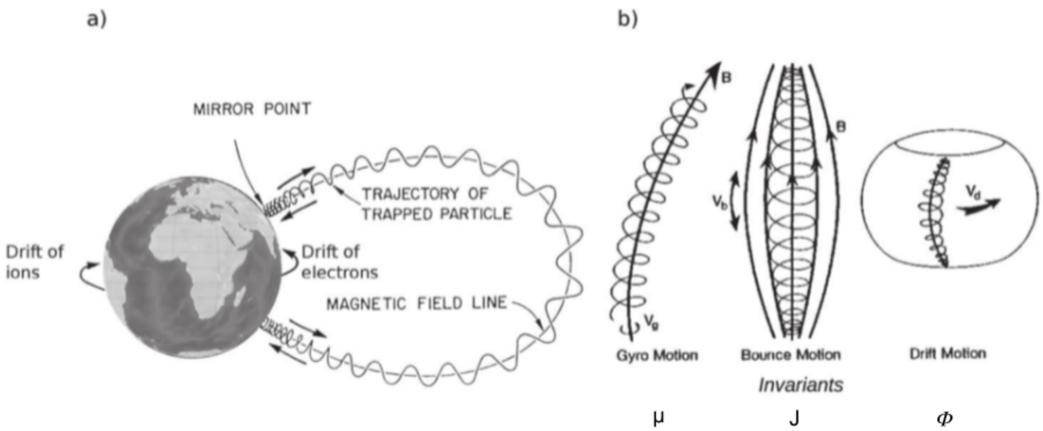

Figure 2.2: (a) Diagram of guiding center approximated bounce motion along a magnetic field line. (b) Visualization of the three adiabatic invariants. From right to left, gyro, bounce, and drift orbits for electrons (figure adapted from Regi 2016).

2.3.1 Gyromotion and the Magnetic Moment

We discussed in Section 2.1 that a charged particle in a magnetic field will gyrate around a field line. This motion has an associated perpendicular kinetic energy and magnetic field strength that governs the gyroradius and the gyrofreqeuncy. The ratio between these two quantities defines the magnetic moment μ,

$$\mu = \frac{mv_\perp^2}{2B} \tag{2.15}$$

μ is considered invariant only when the magnetic field varies slowly over time compared to the gyroperiod and when the change in the gradient of the magnetic field is small. These two assumptions allow us to model the gyromotion of the particle as being a closed orbit, in the absence of an electric field.

In the case of an electric field, μ can still be conserved. This has already been hinted at in mentioning magnetic fields varying in time. The same restrictions apply as with magnetic fields, temporal and spacial variations must be smaller than the variations associated with the particle. For a full derivation, see Section 2.5 in Baumjohann and Treumann 1997.

The conservation of μ is crucial in guiding center approximations. This approximation averages a particles trajectory over a full gyroperiod in order to reduce computational time. This is particularly valuable when computing backwards traces using large numbers of particles.

2.3.2 Bounce Motion and the Longitudinal Invariant

We now move on to look at the motion of charged particles along the Earth's magnetic field lines. Assuming that a particle has a non-zero parallel velocity the particle will move through an inhomogeneous magnetic field as it moves off of an equatorial position. Since the particle's total energy cannot change, if $E = 0$, the only way for μ to hold constant is if the direction of the velocity changes.

This brings us back to our discussion of mirroring particles at our reflection point. This reflection occurs in both the Northern and Southern hemisphere. Over time the particle will continue to bounce back and forth between these two points, called mirror points. However, if the particle penetrates deeply enough into the ionosphere, it will be lost due to collisions with neutral particles. This can lead to certain types of aurora. The invariant associated with this bounce motion is called the longitudinal or second invariant.

The longitudinal invariant is defined as,

$$J = \oint m v_{\|} ds \tag{2.16}$$

where m is the mass of the particle and ds is a line segment along the magnetic field. Note that there can be discrepancy between different definitions of J, with some including a factor of 2 and removing the mass. J is conserved as long as the bounce period is shorter than variations in the magnetic field.

The bounce period, τ_b, is defined as the time it takes a particle to leave the equatorial plane bounce off of both mirror points and return to the plane and is calculated from,

$$\tau_b = 2 \int_{-sm}^{+sm} \frac{ds}{v_{\|}(s)} \tag{2.17}$$

with $\pm sm$ representing the northern and southern mirror point, respectively [Roederer 1970].

2.3.3 Drift Motion and Magnetic Flux

As previously mentioned, the gradient and curvature drift combine to form the total magnetic drift. This drift is in the azimuthal direction around the Earth and is associated with the third adiabatic invariant. The inclusion of charge in both of these drifts means that ions and electrons will orbit in opposite directions, resulting in the westward ring current. Taking a surface of fixed area, S, we can calculate the magnetic flux, Φ, at a given radial distance using,

$$\Phi = \oint d\mathbf{S} \cdot \mathbf{B} \tag{2.18}$$

However, for single particle motion the magnetic flux can be derived another way.

As the particles precess around the Earth, assuming a constant field, they will complete a full orbit in some time, τ_d, and assuming that the path is circular we can calculate the average drift velocity as

$$\langle v_d \rangle \approx \frac{6L^2W}{qB_ER_E} 3LW(0.35 + 0.15 \sin \alpha_{eq}) \tag{2.19}$$

where B_E and R_E are the equatorial magnetic field strength at the surface of the Earth and the Earth's radius respectively and α_{eq} is the pitch angle measured at the equator. From this we can relate the magnetic flux to the drift velocity by,

$$\Phi = \oint v_d r d\phi \tag{2.20}$$

This invariant has the longest time scale associated with it as drift periods tend to be on the order of days while bounce periods are on the order of minutes for protons and the gyroperiod is on the order of seconds for ions. These values will vary depending on the energy and radial distance of the particle.

Chapter 3

Magnetohydrodynaimcs and ULF Waves

All of the equations previously defined focus on single-particle dynamics. Unfortunately, as we begin to study large populations of particles, not only does the computational time required for these calculations make a single-particle approach unrealistic, the results will not account for the interactions between particles. In order to correctly model larger populations, we must move over to a magnetohydrodynamic (MHD) model.

3.1 The Foundations of MHD

MHD is a continuum approach to viewing plasma dynamics that gets its name from the two foundations that the theory is based on, hydrodynamics and electromagnetism. The elctromagnetism has been introduced in the previous chapter but the hydrodynaimc aspect is just as important. We will be treating the plasma as a conductive fluid and will use this assumption to derive equations for mass density and other fluid dynamics. Before we jump into the equations that make up the core of this theory, we will begin by looking at the assumptions that underlie it. The first assumption is that the plasma can be considered quasi-neutral, meaning that the average number of ions and electrons are the same. Obviously, there must be regions where the charge is non-zero so we want to find the minimum distance where this assumption is accurate. This length is called the Debye length, λ_D and is defined as,

$$\lambda_D = (\frac{\epsilon_0 k_B T_e}{n_e e^2})^{1/2} \tag{3.1}$$

where ϵ_0 is the free space permittivity constant, T_e is the electron temperature, k_B is the Boltzmann constant, n_e is the plasma density and e is the electron charge. As long as we look at length scales longer than the Debeye length we can trust that the plasma is quasinuetral.

For the other two limits that we place on MHD calculations, we return to Section 2.3.1 and the first invariant. As long as changes in the system occur on frequencies lower than the ion gyrofrequency and spatial scales longer than the ion gyromotion, we can use MHD to model our plasma.

3.1.1 Electrodynamics in MHD

The fundamental equations that we will be using for an MHD model come from electrodynamics and hydrodynamics. We will start with Maxwell's equations for the electrodynamics portion,

$$\nabla \times \mathbf{E} = -\frac{\partial \mathbf{B}}{\partial t} \tag{3.2}$$

$$\nabla \cdot \mathbf{E} = \frac{\rho}{\epsilon_0} \tag{3.3}$$

$$\nabla \times \mathbf{B} = \mu_0(\mathbf{j} + \epsilon_0 \frac{\partial \mathbf{E}}{\partial t}) \tag{3.4}$$

$$\nabla \cdot \mathbf{B} = 0 \tag{3.5}$$

Where $\mathbf{E}$ and $\mathbf{B}$ are the electric and magnetic field vectors, $\mathbf{j}$ is the current density, ρ is the charge density, and ϵ_0 and μ_0 are the permittivity and permeability of free space, respectively. For space plasma, we will make a few simplifications to these equations starting with Equation 3.3. The quasinuetral requirement requires that the the plasma is neutrally charged, giving us,

$$\nabla \cdot \mathbf{E} = 0 \tag{3.6}$$

Previous calculations (Allan and Poulter 1992) have shown that as long as our MHD limiting behavior is true, $\mid \nabla \times \mathbf{B} \mid \gg \frac{\partial \mathbf{E}}{\partial t}$, and we can reduce Equation 3.4 to,

$$\nabla \times \mathbf{B} = \mu_0 \mathbf{j} \tag{3.7}$$

In order to study the changes in the current, we will look at the generalized form of Ohm's law for a single-fluid magnetohydrodynamic plasma as derived in Baumjohann and Treumann 1997,

$$\mathbf{E} + \mathbf{v} \times \mathbf{B} = \eta \mathbf{j} + \frac{1}{n_e} \mathbf{j} \times \mathbf{B} - \frac{1}{n_e} \nabla \cdot \mathbf{P}_e + \frac{m_e}{n_e e^2} \frac{\partial \mathbf{j}}{\partial t} \tag{3.8}$$

The first term on the right is the resistive term, where η is the plasma resistivity. The second term is the Lorentz force term or Hall term, where n_e is the electron number density. The third term is the anisotropic electron pressure term, where $\mathbf{P}_e$ is the electron pressure. The final term is the contribution of electron inertia to the current flow, where m_e is the mass of an electron.

Fortunately, we can make some simplifying assumptions. We start by assuming that we are working with a near infinitely conductive plasma so the first term can be eliminated. This is valid as long as we are not looking at regions close to the ionosphere. As long as variations in the plasma occur much more slowly than the gyroperiod of ions in the plasma, we can also eliminate the second and fourth term. Finally, the pressure gradient term must be similar in magnitude to the Hall term to prevent the plasma for reducing to a simple hydrodynamic system, so it can also be ignored. This leaves us with our simplified Ohm's law,

$$\mathbf{E} = -\mathbf{v} \times \mathbf{B} \tag{3.9}$$

This equation is often called the hydromagnetic theorem or more colloquially, the frozen-in flux theorem. The equation shows that, if we take a reference frame moving along with the plasma, the electric field is zero and plasma elements are fixed to the field lines. Alternatively, it can be shown that this theorem is in agreement with flux-conservation.

3.1.2 Hydrodynamics in MHD

The next set of equations come from hydrodynamics. The three main equations that we need are the continuity equation,

$$\frac{\partial \rho_m}{\partial t} + \nabla \cdot (\rho_m \mathbf{v}) = 0 \tag{3.10}$$

which ensures that the mass, is conserved, the equation of motion,

$$\rho_m(\frac{\partial \mathbf{v}}{\partial t} + \mathbf{v} \cdot \nabla \mathbf{v}) = \mathbf{j} \times \mathbf{B} - \nabla p \tag{3.11}$$

which relates the flow of the plasma to the change in plasma pressure and electromagnetic forces, and the equation of state,

$$\frac{p}{\rho^{\gamma_s}} = constant \tag{3.12}$$

which, with Equation 3.9 closes the set of equations for MHD where $\mathbf{v}$ is the fluid velocity of the plasma, ρ_m is the mass density, p is the plasma pressure, and γ_s is the adiabatic index, which can be set to 5/3 for adiabatic cases.

3.2 Waves in MHD

We will now use these equations to study and classify waves within the limits of MHD. We will start by linearizing Maxwell's equations by splitting each term into a background term, denoted by a subscript 0, and a small perturbation term, denoted by a subscript 1. However, our previous assumptions about our plasma allow us to eliminate E_0, j_0 and v_0, resulting in,

$$\begin{aligned} \rho &= \rho_0 + \rho_1 \\ \mathbf{B} &= \mathbf{B}_0 + \mathbf{B}_1 \\ \mathbf{E} &= \mathbf{E}_1 \\ \mathbf{j} &= \mathbf{j}_1 \\ \mathbf{v} &= \mathbf{v}_1 \end{aligned} \tag{3.13}$$

The following sections regarding MHD wave equations are based heavily on the work done by Allan and Poulter 1992. Their derivation of the field equations is followed with additional justification for certain steps in the process.

3.2.1 Cold Plasma Waves

If we take the cold plasma approximation making the plasma pressure, $p = 0$, and neglecting the change in the electric field as it occurs much more slowly than the speed of light, we can rewrite Equation's 3.2, 3.7, and 3.11 as,

$$\nabla \times \mathbf{E}_1 = -\frac{\partial \mathbf{B}_1}{\partial t} \tag{3.14}$$

$$\nabla \times \mathbf{B}_1 = \mu_0 \mathbf{j}_1 \tag{3.15}$$

$$\rho_0 \frac{\partial \mathbf{v}_1}{\partial t} = \mathbf{j}_1 \times \mathbf{B}_0 \tag{3.16}$$

Combining Equations 3.15 and 3.16 and including 3.9 we get,

$$\frac{\partial \mathbf{E}_1}{\partial t} = \frac{(\nabla \times \mathbf{B}_1) \times \mathbf{B}_0}{\rho_0} \tag{3.17}$$

Taking the derivative of both sides with respect to time and using Equation 3.14 gives us the wave equation,

$$\frac{\partial^2 \mathbf{E}_1}{\partial t^2} + v_A^2 \nabla \times (\nabla \times \mathbf{E}_1) = 0 \tag{3.18}$$

Where $v_A = \mathbf{B}_0/\sqrt{\mu_0 \rho_0}$ is the Alfvén speed. We will now use a standard Cartesian coordinate system with a uniform background magnetic field in the $\hat{z}$ direction in order to rewrite Equation 3.2.1 as,

$$\left(\frac{1}{v_A^2}\frac{\partial^2}{\partial t^2} - \frac{\partial^2}{\partial x^2} - \frac{\partial^2}{\partial z^2}\right)E_y = -\frac{\partial^2 E_x}{\partial x \partial y} \tag{3.19}$$

$$\left(\frac{1}{v_A^2}\frac{\partial^2}{\partial t^2} - \frac{\partial^2}{\partial y^2} - \frac{\partial^2}{\partial z^2}\right)E_x = -\frac{\partial^2 E_y}{\partial x \partial y} \tag{3.20}$$

In order to solve these two equations we will need to define the form of the perturbed quantities. Using the plane-wave form, $\exp i(k_y y + k_z z - \omega t)$ and noting that because we have not defined out coordinate system a priori, we can align our axes with the y component of the electric field, ensuring that $\partial/\partial x = 0$ we find that the dispersion relation for Equations 3.19 and 3.20 are,

$$\frac{\omega^2}{k_z^2} = v_A^2 \tag{3.21}$$

$$\frac{\omega^2}{k^2} = v_A^2 \tag{3.22}$$

with $k = \sqrt{k_y^2 + k_z^2}$. These two dispersion relations relate to two different wave modes for the cold plasma case.

Equation 3.21 has a phase velocity of $w/k_z = v_A$ and a group velocity of $\pm v_A \hat{\mathbf{z}}$. Because the group velocity is limited to the z-axis, the flow of energy for this wave mode must travel along the background field. This type of wave is known as a shear Alfvén wave, with shear meaning that the wave experiences transverse perturbations, not compressional ones, and Alfvén after Hannes Alfvén, the first to propose the existence of such waves (Alfvén 1942). If the wave vector $\mathbf{k}$ is not completely aligned with the background field, the current will have some component along the field because the current and k-vector must be orthogonal. This means that oblique waves generate field aligned currents.

The second dispersion relation, Equation 3.22, corresponds to the fast magnetoacoustic mode and has a phase velocity of v_A and a group velocity $\pm v_A \hat{\mathbf{k}}$ meaning that the wave travels by compressing orthogonal to the field direction. While the fast mode dispersion relation can be equal to the Alfvén mode dispersion relation when $k_y = 0$ the orthogonal condition on $\mathbf{j}$ and $\mathbf{B}_0$ means that no field aligned currents can be generated by the fast mode. In the uniform cold plasma model it is clear that the two modes we have derived are uncoupled. Figure 3.1 is included to help visualize the direction of the components in the two modes.

3.2.2 Warm Plasma Waves

If the plasma is no longer cold, the plasma pressure now takes on a finite equilibrium pressure, p_0 that we introduce to Equation 3.16. Because the temperature is now non-zero we are forced to account for the sound speed of the plasma given by,

$$c_s = \sqrt{\frac{\gamma_s P_0}{\rho_0}} = \sqrt{\frac{\gamma k_B T}{m}} \tag{3.23}$$

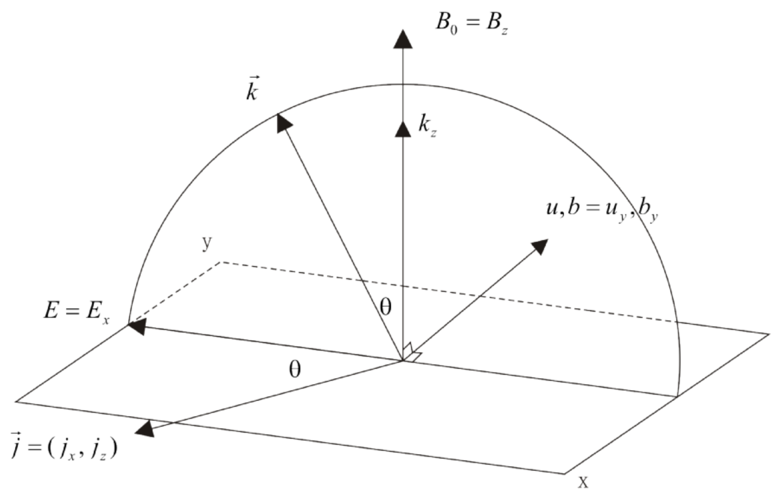

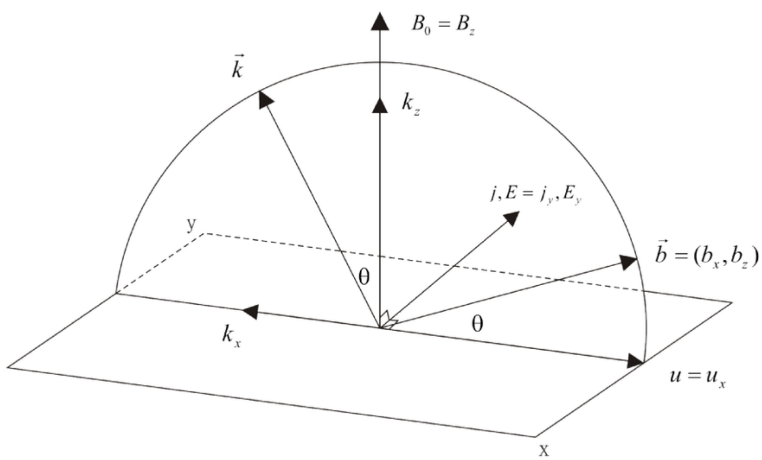

Figure 3.1: Relative directions of different components r different modes. Upper Panel: The shear Alfvén mode. Lower Panel: The fast mode. (Allan and Poulter 1992)

where γ_s is the ratio of the specific heats, k_B is Boltzmann's constant and P_0 is the pressure. The Alfvén mode is unaffected by this change but the fast mode dispersion relation, Equation 3.22, is split into two equations,

$$\frac{\omega^2}{k^2} = \frac{c_s^2 + v_A^2}{2}\left[1 \pm \sqrt{1 - \frac{4c_s^2 v_A^2 \cos^2\theta}{(c_s^2 + v_A^2)^2}}\right] \tag{3.24}$$

where θ is the angle between the wave vector $\mathbf{k}$ and the background magnetic field $\mathbf{B}_0$. If the wave is propagating along the magnetic field then $\theta = 0$ and the solutions to Equation 3.2.2 are,

$$\frac{\omega}{k} = v_A^2 \tag{3.25}$$

$$\frac{\omega}{k} = c_s^2 \tag{3.26}$$

The first has the same form as the fast mode from the cold plasma case and is defined as the transverse fast mode and the second is a compressional sound wave. For the opposite limit, where $\mathbf{k}$ and $\mathbf{B}_0$ are nearly perpendicular, $\theta \simeq 90°$, the two solutions now take the form,

$$\frac{\omega^2}{k^2} \simeq c_s^2 + v_A^2 \tag{3.27}$$

$$\frac{\omega^2}{k^2} \simeq \frac{c_s^2 v_A^2}{c_s^2 + v_A^2} \tag{3.28}$$

As the angle between $\mathbf{k}$ and $\mathbf{B}_0$ increase the magnetic compressional fast mode more easily couples to the fluid compressional sound wave with two dispersion relations. These two dispersion relations are tied to the fast, Equation 3.27 and slow, Equation 3.28, magnetosonic modes. The difference between the two modes has to do with the coupling between the magnetic and fluid pressure perturbations. In the fast mode, these two perturbations are in phase and for the slow mode they tend to cancel each other out.

It is clear that as the temperature approaches zero the fast magnetosonic mode will decrease in speed until it is once again described by the fast mode. The slow mode behaves similarly to the shear Alfvén mode with energy flowing along the

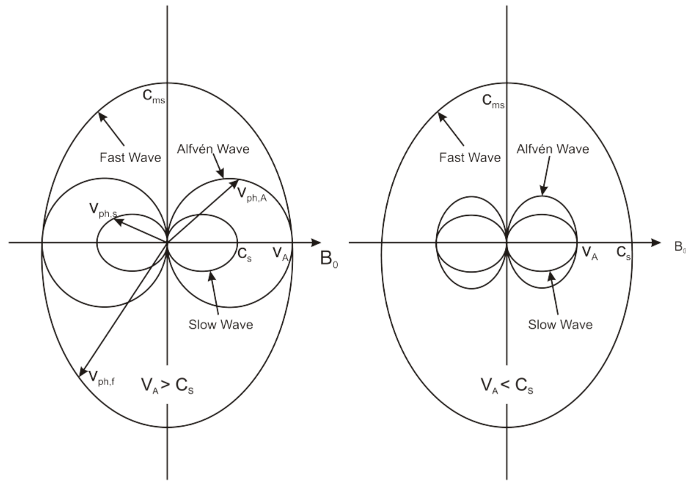

Figure 3.2: Variation in the phase velocity between the fast, slow, and Alfvén mode resulting from alignment of $\mathbf{k}$ and $\mathbf{B}_0$ (Baumjohann and Treumann 1997).

background field direction. However, neither the fast nor slow magnetosonic modes interact with the shear Alfvén mode when the plasma is uniform. A comparison of the velocities between the fast mode, slow mode and Alfvén mode are shown in Figure 3.2 for two cases, $v_A > c_s$ and $v_A < c_s$.

3.2.3 Field Line Resonance

We will now look at how these waves can interact with the Earth's natural magnetic field and how they can transport energy from the solar wind to the inner magnetosphere where the plasma is non-uniform. In order to do this, we will start with a box model representation of the Earth's magnetosphere, Figure 3.3. The upper and lower boundaries correspond to the footprints of the magnetic field lines in the ionosphere, which we will assume are fixed. The left side is the ionosphere and the right side is the magnetopause, where our waves will be entering from.

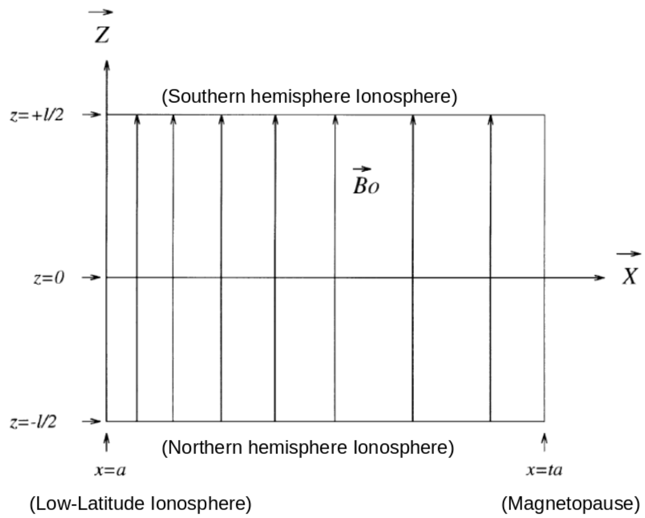

Figure 3.3: Box model of dipole field lines. Waves will travel in from the right side of the diagram. (Cheng, Chao, and Hsu 1998).

This model features an overall gradient in the magnetic field in the x direction, increasing towards the Earth. We do assume that the field lines have a constant length which ensures that any variation in the Alfvén speed is due to the changes in the magnetic field and the plasma density.

We begin by explicitly writing out the x-dependence of our new model into our Alfvén speed and the E_x and E_y,

$$
\begin{aligned}
v_A &= v_A(x) \\
E_x &= E_x(x)exp[i(k_y y + k_z z - \omega t)] \\
E_y &= E_y(x)exp[i(k_y y + k_z z - \omega t)]
\end{aligned}
\tag{3.29}
$$

and then rewriting Equations 3.19 and 3.20,

$$
\Big(\frac{\omega^2}{v_A^2(x)} - k_y^2 - k_z^2\Big)E_x = ik_y\frac{dE_y}{dx} \tag{3.30}
$$

$$\Big(\frac{\omega^2}{v_A^2(x)}-k_z^2\Big)E_y = ik_y\frac{dE_x}{dx}-\frac{d^2E_y}{dx^2} \tag{3.31}$$

If we assume that the wave vector has no y-component we can decouple the E_x and E_y terms to get,

$$\Big(\frac{\omega^2}{v_A^2(x)}-k_z^2\Big)E_x = 0 \tag{3.32}$$

$$\Big(\frac{\omega^2}{v_A^2(x)}-k_z^2\Big)E_y = -\frac{d^2E_y}{dx^2} \tag{3.33}$$

Where Equation 3.32 corresponds to the shear Alfvén mode as shown in Equation 3.19. Similarly, Equation 3.33 is related to Equation 3.20 with the addition of a spatial variation in the x direction. We assume that the ratio, $\omega^2/v_A^2(x)$ is increasing monotonically with x. An important characteristic of these new equations is the relationship between $\omega^2/v_A^2(x)$ and k_z^2 in Equation 3.33. There must be some critical value, x_r where the ratio between the frequency and Alfvén speed is equal to k_z^2. This value of x is known as the turning point or reflection point, where the refractive index of the magnetosphere goes to zero. Here the fast mode waves associated with E_y will reflect while their evanescent component continues past this point towards the Earth's ionosphere. This reflection can result in radially standing structure if the reflected wave is once again reflected at some point $x > x_r$ which can occur at the magnetopause.

However, these solutions are only for the special case where $k_y = 0$, we will now look at the behavior of these waves for the case of general k_y. Now we can combine Equations 3.30 and 3.31 to get,

$$C = \frac{k_y^2\omega^2 dv_A^{-2}(x)/dx}{(\omega^2/v_A^2(x)-k_z^2)(\omega^2/v_A^2(x)-k_y^2-k_z^2)} \tag{3.34}$$

We still have a turning point at x_r due to the right hand side of the denominator but the left hand side also gives us a new point of interest, x_c where $\omega^2/v_A^2(x) = k_z^2$.

The new point x_c must be closer to the ionosphere than x_r since we have assumed a non-zero k_y. At x_c the phase velocity of the fast mode wave in the field aligned direction is equal to the local Alfvén phase velocity. This allows energy to transfer from the inward traveling fast mode waves to standing Alfvén waves.

This interaction is known as field line resonance and is illustrated in Figure 3.4. As an incident fast mode wave approaches the Earth from the magnetosphere it will eventually reach the reflection point, labeled x_t in the figure, where the fast mode will reflect but the evanescent portion of the wave continues towards the Earth. As this portion of the wave moves closer to the Earth the frequency of the standing Alfvén waves increase. At the resonance point, labeled x_r in the figure, the frequencies between these two waves match and energy can be transferred to the wave, denoted by a large peak in the magnitude of B_y. This concludes the summary of MHD wave behavior outlined by Allan and Poulter 1992.

3.3 Drift and Drift Bounce Resonance

As electrons and ion drift around the Earth in the Van Allen belts they interact with wave fields. This interaction was first outlined by Southwood, J. Dungey, and Etherington 1969, who discussed the possible energy transfer between field line resonances (FLR) and drifting particles. The basic idea is analogous to pushing a child on a swing. As energetic particles orbit around the Earth they may be accelerated by a poloidal mode with an electric field parallel to the particles drift motion. If the FLR "pushes" the particles at the right speed the particles will gain a large amount of energy. This condition is embodied by the drift-bounce resonance equation,

$$\omega - m\omega_d = N\omega_b \tag{3.35}$$

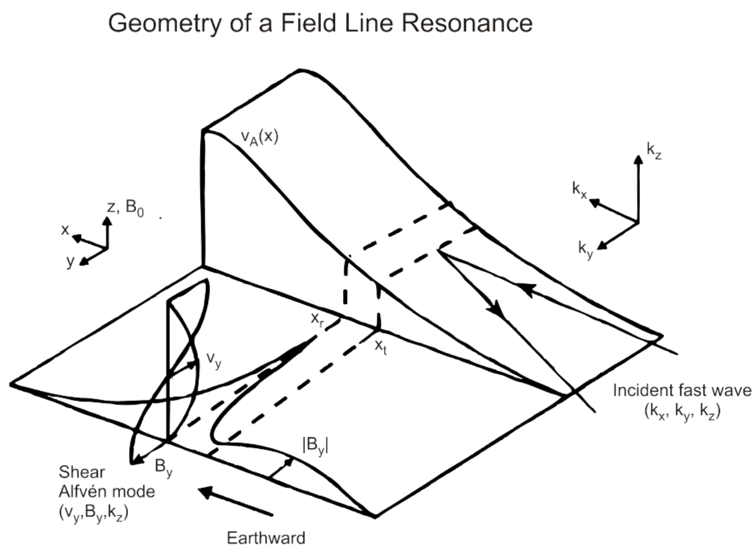

Figure 3.4: Figure showing the increase in the Alfvén speed along the x-axis with reflection point marked as x_t and the resonance location is labeled as x_r. Z is the field-aligned direction and y is the azimuthal direction (Rankin, Samson, and Frycz 1993).

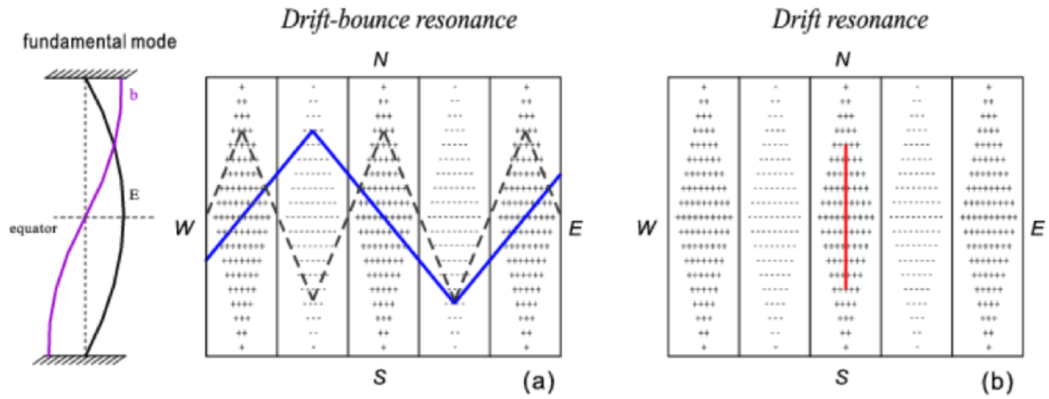

Figure 3.5: Drift and Drift Bounce resonance for a fundamental mode ULF wave. (Yang et al. 2011)

where ω is the frequency at which the FLR is driven, m is the azimuthal wave number of the wave, ω_d and ω_b are the drift and bounce frequencies of the particle, and N is an integer representing the number of wavelengths covered over a full bounce period.

The simplest form of this resonance occurs where the azimuthal velocity of the particle is identical to that of the wave, resulting in drift motion, $N = 0$. This drift motion is similar to a surfer riding a wave. If the surfer has to travel at the speed of the wave in order to stay on top of it. As long as the particle stays in-phase with the wave it will continue to gain energy, as shown in (b) of Figure 3.5. The positive and negative signs correspond to a positive and negative electric field, with the density of the signs representing the strength of the field. In this case the particle will gain the most energy at the equator. The resonance energy associated with a given wave for fundamental drift resonance is,

$$W_{res} = \frac{\omega R_e^2 q B_e}{3mL} \tag{3.36}$$

where ω is the wave frequency, B_e is the earth's magnetic field, and m is the azimuthal wave number.

But drift resonance is a special condition and in general the particle's velocity will not match perfectly with the wave. Even when it does, the energization will cause the velocity to change and the particle will begin traveling through regions of varying electric field as shown in (a) of Figure 3.5. The dotted line shows a case where the particle experiences a symmetric positive and negative acceleration over one bounce period as it gains energy in the first half and loses the energy in the second half, resulting in no net change in energy. The blue shows the case for a positively accelerated particle. As the particle moves through the positive field, it is close to the equator and experiences a large positive acceleration. It enters the negative potion of the field off the equator where the acceleration is weaker. This results in a positive net change in energy over a bounce period.

If the particle population has a lower average energy than the wave the ULF waves accelerates more particles than it decelerates. This results in an overall increase in the particles energy from the wave. The reverse can also occur, whereby the wave gains energy from interacting with the particles. This process is a potential source of giant pulsation events in the inner magnetosphere (Green 1979; Green 1985).

Chapters 2 and 3 have outlined the fundamental equations for particle dynamics and the definitions and behaviors of MHD waves. This theoretical background will be used in Chapters 4 and 5. The dipole field model and adiabatic invariants, outlined in Chapter 2, will have a key role in the modeling of the particle trajectories in Chapter 5. The MHD wave assumptions previously discussed in this chapter will be used to derive new field equations for poloidal mode Alfvén waves in the next chapter.

Chapter 4

Poloidal Mode Wave Model

This chapter will describe the analytic ULF mathematical model that is used for the simulations that make up the rest of this thesis. We outline the dipole coordinate system that we used before going into detail about the assumptions used in defining the fields. Previous derivations of the field components have used a finite difference calculation for the compressional field. Here, we show one derivation of a fully analytic poloidal field model. This model is compared with a similar model (C. Wang, Rankin, Y. Wang, et al. 2018).

4.1 Analytic ULF Wave Model

We start by defining the coordinate system that we will be using in the derivation of our fields. We also provide a justification for assuming an infinitely conductive ionosphere. We first derive the wave equation for the poloidal mode wave. A driver term is introduced and analytic solutions for the electric and magnetic fields are calculated.

4.1.1 Dipole Coordinate System

As previously mentioned, the Earth's magnetic field can be approximated as a dipole and we have already made use of this in our calculation of drifts. However, in solving for a set of analytic solutions to the dipole field it will benefit us to use a dipole coordinate system x_1, x_2, x_3 as previously defined (Radoski 1967; Swisdak 2006), in terms of spherical polar coordinates (r, θ, ϕ),

$$\begin{aligned} x_1 &= \frac{\cos\theta}{r^2} \\ x_2 &= \frac{r}{\sin^2\theta} \\ x_3 &= \phi \end{aligned} \tag{4.1}$$

where r is the radial distance from the center of the Earth divided by the Earth's radius, θ is colatitude, and ϕ is the longitude direction. For a dipole coordinate system x_1 is along the field line, x_2 is radial, and x_3 is longitudinal. x_1 and x_3 are also referred to as the compressional and azimuthal direction, respectively. The metric terms associated with this orthogonal coordinate system are,

$$\begin{aligned} h_1 &= \frac{r^3}{\sqrt{1+3\cos^2\theta}} \\ h_2 &= \frac{r^2}{\sqrt{1+3\cos^2\theta}\sin\theta} \\ h_3 &= r\sin\theta \end{aligned} \tag{4.2}$$

We will also define frequently used vector operations using generalized curvilinear definitions. Here the divergence is defined as,

$$\nabla\cdot\mathbf{F} = \frac{1}{h_1h_2h_3}\Big[\frac{\partial(F_1h_2h_3)}{\partial x_1} + \frac{\partial(h_1F_2h_3)}{\partial x_2} + \frac{\partial(h_1h_2F_3)}{\partial x_3}\Big] \tag{4.3}$$

for a general vector F, and the curl is,

$$\nabla \times \mathbf{F} = \frac{1}{h_1 h_2 h_3} \begin{vmatrix} h_1\mathbf{e}_1 & h_2\mathbf{e}_2 & h_3\mathbf{e}_3 \\ \partial/\partial x_1 & \partial/\partial x_2 & \partial/\partial x_3 \\ h_1 F_1 & h_2 F_2 & h_3 F_3 \end{vmatrix}$$

The above definition of dipole coordinates and metric terms can be rewritten in terms of the the field line position, $s = \cos\theta$ and the mirror point location, $s_m = \sqrt{1 - 1/L}$.

4.1.2 Decoupling the Poloidal and Toroidal Mode

The toroidal and poloidal modes refer to two different polarizations of the wave and are distinguished by the electric field component associated with each. The toroidal mode corresponds to the radial electric field, E_2 and the the poloidal mode corresponds to the azimuthal electric field, E_3. These three fields are components of the field while the mode classifies them collectively. Previous research (Allan and Knox 1979) found evidence that these two modes interact through the ionosphere via the Hall current.

The ionosphere has a finite conductivity meaning that the "frozen-in" condition discussed in Section 3.1.1 is not valid. As such, we are forced to consider the currents associated with the Hall and Pedersen conductivity, labeled as σ_H and σ_P respectively. These currents can be written as,

$$\begin{aligned} j_2 &= \sigma_P E_2 + \sigma_H E_3 \\ j_3 &= \sigma_P E_3 + \sigma_H E_2 \end{aligned} \tag{4.4}$$

Using Equation 3.7 and integrating from the bottom to the top of the ionosphere along the field line we find,

$$\pm\frac{1}{\mu_0}B_3^0 = \Sigma_P E_2^0 + \Sigma_H E_3^0$$
$$\mp\frac{1}{\mu_0}(B_2^0 - B_2^1) = \Sigma_P E_3^0 + \Sigma_H E_2^0 \tag{4.5}$$

where Σ_H and Σ_P the height-integrated conductivity and the superscripts 0 and 1 refer to the top and bottom of the ionosphere, respectively. We have also assumed that $B_3^1 = 0$ as the displacement currents below the ionosphere are negligible over wave periods in the Pc 3-5 range (2-100 mHz). The upper symbols in these equations are used for calculations in the southern hemisphere and the lower symbols are used for the northern hemisphere. Using Equation 3.14, it is clear that the E_2 and E_3 terms are coupled,

$$\pm\frac{i}{\mu_0\omega}\left[\frac{1}{h_1h_2}\frac{\partial}{\partial x_1}(h_2E_2)\right]^0 = \Sigma_P E_2 + \Sigma_H E_3$$
$$\mp\frac{1}{\mu_0}\left\{\frac{i}{\omega}\left[\frac{1}{h_2h_3}\frac{\partial}{\partial x_1}(h_3E_3)\right]^0 + B_2^1\right\} = \Sigma_P E_3 + \Sigma_H E_2 \tag{4.6}$$

These two equations are decoupled when the Hall conductivity is assumed to be zero. This assumption is used in our model in order to simplify the derivation of the fields.

4.1.3 Free wave Equation for the Poloidal Mode Alfvén Wave

The poloidal mode is made up of the compressional magnetic field (B_{11}), radial magnetic field (B_2), and the azimuthal electric field (E_3) with subscripts corresponding to the coordinate system defined above. The compressional magnetic field is defined as such to prevent confusion with the background magnetic field (B_{10}) and the total magnetic field along the field lines (B_1). Starting from Faraday's law we can focus on the radial component,

$$[\nabla \times (\mathbf{v} \times \mathbf{B})]_2 = \frac{\partial B_2}{\partial t} \tag{4.7}$$

We can then use Equation 4.1.1 to expand this as,

$$[\nabla \times E]_2 = \frac{1}{h_1 h_2 h_3}[\frac{\partial}{\partial x_1}(h_3 E_3) - \frac{\partial}{\partial x_3}(h_1 E_1)]h_2 \hat{e_2} \tag{4.8}$$

Using the definition of the poloidal mode we can remove the second term on the right hand side as $E_1 = 0$. The first term can be rewritten, using Equation 3.9 and noting that $v_1 = 0$, we obtain,

$$E_3 = v_2 B_1 \tag{4.9}$$

Finally we can multiply both sides by h_2 and substituting our fields into Faraday's Law yields,

$$\frac{h_2 \partial B_2}{\partial t} = \frac{h_2}{h_1 h_3}\frac{\partial}{\partial x_1}(h_3 v_2 B_{10}) \tag{4.10}$$

We will use the poloidal mode components of the equation of motion, Equation 3.11, assuming that the change in plasma pressure is negligible,

$$\rho \frac{\partial v_2}{\partial t} = \frac{(\nabla \times B_1) \times B_{10}}{4\pi} \tag{4.11}$$

By simplifying the right hand side and multiply both sides by $h_3 B_{10}/\rho$ we get,

$$\frac{\partial}{\partial t}(h_3 B_{10} v_2) = \frac{v_A^2 h_3}{h_1 h_2}\frac{\partial}{\partial x_1}(h_2 B_2) \tag{4.12}$$

where $v_A = B_{10}/\sqrt{\mu_0 \rho_0}$ is the Alfvén speed. We can then combine Equation 4.10 with the time derivative of Equation 4.12 to get

$$\frac{\partial^2}{\partial t^2}(h_2 B_2) = \frac{1}{h_3^2}\frac{\partial}{\partial x_1}\frac{v_A^2}{h_2^2}\frac{\partial}{\partial x_1}(h_2 B_2) \tag{4.13}$$

The eigenfunction of Equation4.13 is,

$$h_2 B_2 = b_N(x_2,t)\exp i(\omega_N t - m\phi)S_N(x_1) \tag{4.14}$$

Where b_N is the amplitude of the field, ω_N is the eigenfrequency, mϕ corresponds to the azimuthal propagation of the wave, and S_N is the N-th order eigenfunction of the field line resonance. Since we have assumed that the ionosphere is perfectly conductive we can simplify $\partial^2 B_2/\partial t^2$ as $-\omega_N^2$, giving us,

$$\frac{d}{dx_1}[\frac{v_A^2}{h_2^2}\frac{dS_N}{dx_1}] + h_3^2\omega_N^2 S_N = 0 \tag{4.15}$$

In order to normalize the solution to S_N we look at the relationships between different eigenmodes. To do so, we multiply both sides by a different eigenmode, S_M and integrate along the field line,

$$\int_{x_-}^{x_+} dx_1 S_M[\frac{d}{dx_1}(\frac{v_A^2}{h_2^2}\frac{dS_N}{dx_1}) + h_3^2\omega_N^2 S_N] = 0 \tag{4.16}$$

x_- and x_+ correspond to the northern and southern hemispheres, respectively. After integrating by parts we find,

$$\omega_N^2\int_{x_-}^{x_+} dx_1 h_3^2 S_M S_N + S_M\frac{v_A^2}{h_2^2}\frac{dS_N}{dx_1}\Big|_{x_-}^{x_+} - \int_{x_-}^{x_+} dx_1\frac{v_A^2}{h_2^2}\frac{dS_M}{dx_1}\frac{dS_N}{dx_1} = 0 \tag{4.17}$$

This integration is repeated, by switching M to N and subtracting, giving the orthogonality condition,

$$(\omega_N^2 - \omega_M^2)\int_{x_-}^{x_+} dx_1 h_3^2 S_M S_N = Const\cdot\delta_{N,M} \tag{4.18}$$

Therefore, the normalized solution of S_N is,

$$\int_{x_-}^{x_+} dx_1 h_3^2 S_N = 1 \tag{4.19}$$

The eigenfunctions and their eigenfrequencies can be solved numerically using this equation. However, an analytic solution to this equation can also be found.

4.1.4 Analytic Solution to the FLR Wave Equation

To solve for the eigenfunction we start with Equation 4.15. However, we will use a change of variables to express our derivatives in terms of s rather than x_1. However, since we are working in dipole coordinates, $x_1(r,s)$, it is important to be clear about what variable is being held constant during the change.

$$\frac{\partial}{\partial x_1} = \frac{\partial}{\partial s}\Big(\frac{\partial s}{\partial x_1}\Big)_r = \frac{(1-s^2)^2 h_2^2}{r^2}\frac{\partial}{\partial s} \tag{4.20}$$

Now Equation4.15 can be written as,

$$\frac{(1-s^2)^2 h_2^2}{r^2}\frac{\partial}{\partial s}[\frac{v_A^2}{h_2^2}\frac{(1-s^2)^2 h_2^2}{r^2}\frac{\partial S_N}{\partial s}] + h_3^2\omega_N^2 S_N = 0 \tag{4.21}$$

In order to simplify this equation to a simple harmonic oscillator form we need to assume some variation of v_A and S_N. Following methods previously established (C. Wang, Rankin, and Zong 2015), we assume the shape of our profile to be similar to $S_N = A\sin(f_N s + \delta)$, where A and δ are constants and f_N is a normalized frequency. A variety of wave forms were tested but in order to get an analytic solution to the wave equations we used,

$$S_N = \sin\left[f_N(s+s^3)\right] \tag{4.22}$$

We can define our density profile such that $v_A = v_{A0}/(1+3s^2)$, where v_{A0} is the normalized Alfvén speed to simplify our wave equation to,

$$\frac{\partial^2 S_N}{\partial s^2} = -\frac{v_{A0}^2 f_N^2}{LR_e} S_N \tag{4.23}$$

In order to find the value of f_N we look at the boundary conditions on the eigenfunction. At the ionosphere the eigenfunction must equal unity while $s = s_{max}$. In order to satisfy Equation 4.22,

$$f_N = \frac{\pi}{2(s_{max} + s_{max}^3)} \tag{4.24}$$

4.1.5 Poloidal Wave Model with an External Driver

We have previously looked at solving for the free wave equation eigenfunction. However, in order to add energy into the system we must introduce a driver defined as, $D = \rho\omega_N v_D \sin\omega_D t$, where v_D and ω_D are the driver velocity and frequency. We repeat the steps outlined in Section 4.1.3 but with a new momentum equation defined as,

$$\rho\frac{\partial v_2}{\partial t} = \frac{B_{10}}{4\pi h_1 h_2}\frac{\partial}{\partial x_1}(h_2 B_2) + D \tag{4.25}$$

By repeating the steps between Equations 4.11 and 4.12, we find

$$\frac{\partial}{\partial t}(h_3 B_{10} v_2) = \frac{v_A^2}{h_2^2}\frac{\partial}{\partial x_1}(h_2 B_2) + h_3 B_{10}\omega_D v_D \Re(ie^{-i\omega_D t}) \tag{4.26}$$

Using Equation 4.10, we find

$$\frac{\partial^2}{\partial t^2}(h_2 B_2) = \frac{1}{h_3^2}\frac{\partial}{\partial x_1}\left[\frac{v_A^2}{h_2^2}\frac{\partial}{\partial x_1}(h_2 B_2)\right] + \frac{1}{h_2^3}\frac{\partial}{\partial x_2}[h_3 B_{10}\omega_D v_D \Re(ie^{-i\omega_D t})] \tag{4.27}$$

Using our previous definition of the eigenfunction from Equation4.14 and defining $\Delta\omega = \omega_N - \omega_D$, we can rewrite Equation 4.14 as,

$$h_2 B_2 = b_0 \Re(e^{-i\Delta\omega t})\Re(e^{-i\omega_D t})S_N = b_N(t)\Re(e^{-i\omega_D t})S_N \tag{4.28}$$

with $b_N = b_0\Re(e^{-i\Delta\omega t})$ and b_0 is a constant. Assuming that we are looking at behavior near the resonant position we can use $\Delta\omega^2 << \omega_D^2$ to write,

$$-\omega_D b_N(t)S_N - 2i\omega_D\frac{\partial b_N(t)}{\partial t}S_N = \frac{b_N(t)}{h_3^2}\frac{\partial}{\partial x_1}(\frac{v_A^2}{h_2^2}\frac{\partial S_N}{\partial x_1}) + i\frac{\omega_D}{h_3^2}\frac{\partial}{\partial x_1}(h_3 B_{10} v_D) \tag{4.29}$$

This can be simplified by using Equation 4.15 to obtain,

$$-\omega_D b_N(t)S_N - 2i\omega_D\frac{\partial b_N(t)}{\partial t}S_N = -\omega_N^2 S_N b(t)_N + i\frac{\omega_D}{h_3^2}\frac{\partial}{\partial x_1}(h_3 B_{10} v_D) \tag{4.30}$$

Isolating the derivative in the field-aligned direction, multiplying both sides by $h_3^2 S_N$, and integrating along the field line allows us to use Equation 4.19.

$$-\omega_D^2 b_N(t) - 2i\omega_D\frac{\partial b_N(t)}{\partial t} + \omega_N^2 b_N(t) = i\omega_D\int_{x_-}^{x_+} dx_1 S_N\frac{\partial}{\partial x_1}(h_3 B_{10} v_D) \tag{4.31}$$

Integrating by parts and requiring $v_D(x_-) = v_D(x_+) = 0$ leads to,

$$-(\omega_D^2 - \omega_N^2)b_N(t) - 2i\omega_D\frac{\partial b_N(t)}{\partial t} = -i\omega_D\int_{x_-}^{x_+} dx_1 (h_3 B_{10} v_D)\frac{\partial S_N}{\partial x_1} \tag{4.32}$$

We isolate $\frac{\partial b_N(t)}{\partial t}$ to find,

$$\frac{\partial b_N(t)}{\partial t} = \frac{(\omega_D^2 - \omega_N^2)}{-2i\omega_D} b_N(t) + \frac{\omega_D}{2\omega_D} \int_{x_-}^{x_+} dx_1 (h_3 B_{10} v_D) \frac{\partial S_N}{\partial x_1} \tag{4.33}$$

Using the assumption that the area of interest is near the resonance position this reduces to,

$$\frac{\partial b_N(t)}{\partial t} \sim -i\Delta\omega b_N(t) + \frac{\omega_D}{2} R_D \tag{4.34}$$

where $R_D = \frac{1}{\omega_D} \int_{x_-}^{x_+} dx_1 (h_3 B_{10} v_D) \frac{\partial S_N}{\partial x_1}$ and is the amplitude of the driver. It is a constant parameter in our model and is in units of nT. Our next step is to solve for b_0. Assuming $b_N(t=0) = 0$ we find,

$$-i\Delta\omega b_N(t) + \frac{\omega}{2} R_D = \frac{\omega_D}{2} R_D e^{-i\Delta\omega t} \tag{4.35}$$

Isolating $b_N(t)$ and taking the real portion of it leaves,

$$b_N = \frac{\omega_D R_D}{\Delta\omega} \sin\left(\frac{\Delta\omega t}{2}\right) \tag{4.36}$$

4.1.6 Analytic Poloidal Field Equations

Now that we have defined the amplitude of our eigenfunction, we can derive our analytic field equations for the poloidal mode. We begin with a solution for the radial magnetic field. Evaluating Equation 4.14 and converting sin to sinc, which we define as $\operatorname{sinc}(x) \equiv \sin(x)/x$,

$$B_2 = \frac{t\omega_D R_D S_N}{2h_2} \cos(\omega_N t - m\phi) \operatorname{sinc}\left(\frac{\Delta\omega t}{2}\right) \tag{4.37}$$

Since we have assumed that $\Delta\omega^2 << \omega_D^2$ and $\omega_D^2 < 1$, we find that $h_2 B_2 \propto \omega_D t$. This means that the wave will grow linearly with respect to time.

Using Equation 4.10,

$$\frac{\partial}{\partial t}(h_3 B_{10} v_3) = \frac{v_A^2}{h_2^2}\frac{\partial}{\partial x_1}\frac{t\omega_D R_D S_N}{2h_2^2 a}\cos(\omega_N t - m\phi)\,\mathrm{sinc}\,(\frac{\Delta\omega t}{2}) \tag{4.38}$$

and integrating over time we find,

$$-(h_3 B_{10} v_3) = \frac{-v_A^2}{h_2^2}\frac{\frac{1}{2}\omega_D R_D}{\Delta\omega/2}\frac{\partial S_N}{\partial x_1}\frac{\cos(m\phi - \omega_N t + \frac{\Delta\omega t}{2})}{2\omega_D - \Delta\omega} - \frac{\cos(m\phi - \omega_N t - \frac{\Delta\omega t}{2})}{2\omega_D + \Delta\omega} \tag{4.39}$$

Multiplying both sides by h_3 and using Equation 4.9, and simplifying using $\Delta\omega^2 << \omega_D^2$ we get the azimuthal electric field,

$$E_3 = -\frac{v_A^2}{h_2^2 h_3}\frac{t\omega_D R_D}{2}\frac{\partial S_N}{\partial x_1}\sin(\omega_N t - m\phi)\,\mathrm{sinc}\,(\frac{\Delta\omega t}{2}) \tag{4.40}$$

Next, we use the definition of Faraday's Law to find the compressional field, B_{11} based on the azimuthal electric field, E_3 and assuming that the radial electric field, E_2 is zero.

$$\frac{\partial B_{11}}{\partial t} = -\frac{1}{h_2 h_3}\frac{\partial}{\partial x_2}(h_3 E_3) \tag{4.41}$$

where E_3 has been defined as,

$$E_3 = \frac{v_A^2}{h_2^2 h_3}\frac{\omega_D}{\Delta\omega}\frac{\partial S_N}{\partial x_1}\sin(\omega_N t - m\phi)\sin(\frac{\Delta\omega t}{2}) \tag{4.42}$$

In order to make some of the calculations simpler we have returned to the sine form of E_3.

Since the metric factors have no time dependence we can integrate both sides of the Equation and move the integral through the spatial derivative. The Alfvén speed, derivative of the eigenfunction, and the change in frequency are also time independent so we can begin our derivation by integrating the two sine terms in E_3.

$$\int_0^t \sin(\omega_N t - m\phi)\sin(\frac{\Delta\omega t}{2})dt = \\ \frac{1}{\omega_N^2 - \frac{\Delta\omega^2}{4}}[\frac{\Delta\omega}{2}\cos\frac{\Delta\omega t}{2}\sin(\omega_N t - m\phi) - \omega_N \sin\frac{\Delta\omega t}{2}\cos(\omega_N t - m\phi)] \tag{4.43}$$

Here we make an assumption about the form of the wave. We expect the wave to be smooth and finite with a peak at the resonance location. This criteria requires us to have a waveform that can be modeled using the sinc function. This requires us to focus on the second term in brackets.

We can now return to Faraday's law and define our compressional magnetic field as,

$$B_{11} = \frac{t}{2}\frac{1}{h_2 h_3}\frac{\partial}{\partial x_2}[\frac{v_A^2}{h_2^2}\frac{\partial S_N}{\partial x_1}\frac{\omega_N}{\omega_N^2 - \frac{\Delta\omega^2}{4}}\cos(\omega_N t - m\phi)\,\mathrm{sinc}\,\frac{\Delta\omega t}{2}] \tag{4.44}$$

From here we assume that the variation in h_2 dominates, ignoring the variation in the eigenfrequency, the Alfvén speed, and the sinc function. These assumptions are made because in h_2^2 is of higher order than the other terms found in the equation. We also assume that for dynamics near the resonant location , $\Delta\omega << \omega_N$.

$$B_{11} = \frac{4}{h_2 h_3}[\frac{v_A^2}{r^3}\frac{\partial S_N}{\partial x_1}\frac{t\omega_N}{2\omega_N^2}\cos(\omega_N t - m\phi)\cos(1 + 3\cos^2\theta)\,\mathrm{sinc}\,\frac{\Delta\omega t}{2}] \tag{4.45}$$

This definition for B_{11} was then checked using $\nabla \cdot B = 0$. However, this check was done using the same assumptions regarding leading order terms. This means that the check only validates our solution for B_{11} as mathematically correct, not that our assumptions are valid.

4.2 Comparison With Previous Models

We will be comparing the fields derived in the previous section with previous published results (C. Wang, Rankin, Y. Wang, et al. 2018). Both models are derived from the same assumptions of driven linear shear Alfvén Waves (Rankin 2014). The key difference between the two models is that my model uses a fully analytic compressional magnetic field while Wang's uses a finite difference method.

In order to compare our fields, we looked at the variation in the poloidal mode components as a function of latitude. We used the same wave parameters as C. Wang, Rankin, Y. Wang, et al. 2018 including wave-number, wave frequency, and resonance location. The fields are plotted again a quarter of a wave period later to show the time dependent component of the fields and highlight the phase relationship between the components. C. Wang, Rankin, Y. Wang, et al. 2018 did not specify the driver strength or the time at which the figure was captured. We attempted to recreate the fields focusing on the B_1 and E_3 components, however, we were unable to recreate a similar B_2 component.

Figure 4.1 shows the result obtained from the derivation included in this thesis while Figure 4.2 shows the fields published in C. Wang, Rankin, Y. Wang, et al. 2018. Both of these figures show the variation in field strength as a function of latitude. The right column in each figure is a quarter of a wave period later in time.

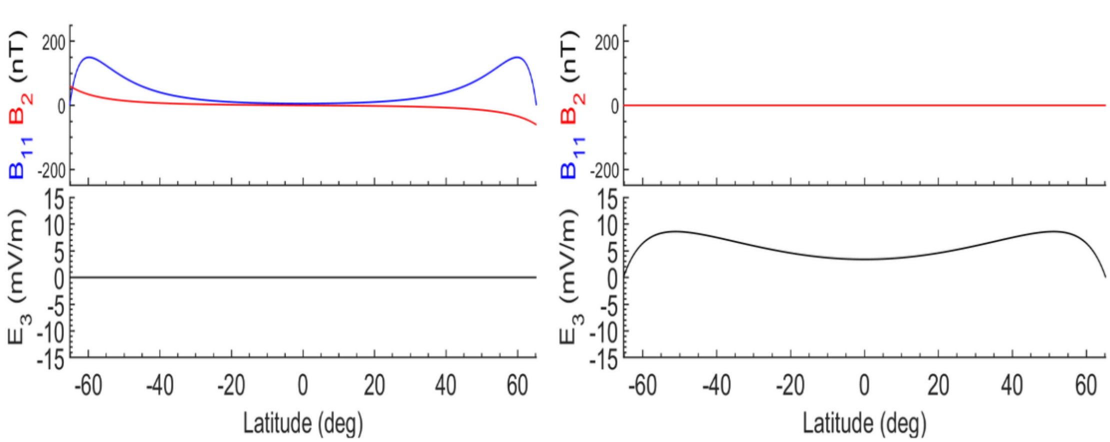

Figure 4.1: Eigenmode for a m = -35, 10mHz poloidal mode excited at L = 5.7 using our model. The fields in the right column are taken a quarter of a wave period after those on the left. The compressional magnetic field (blue) and radial magnetic field (red) are in phase. The magnetic fields (top panels) and azimuthal electric field (bottom panels) are 90 degrees out of phase.

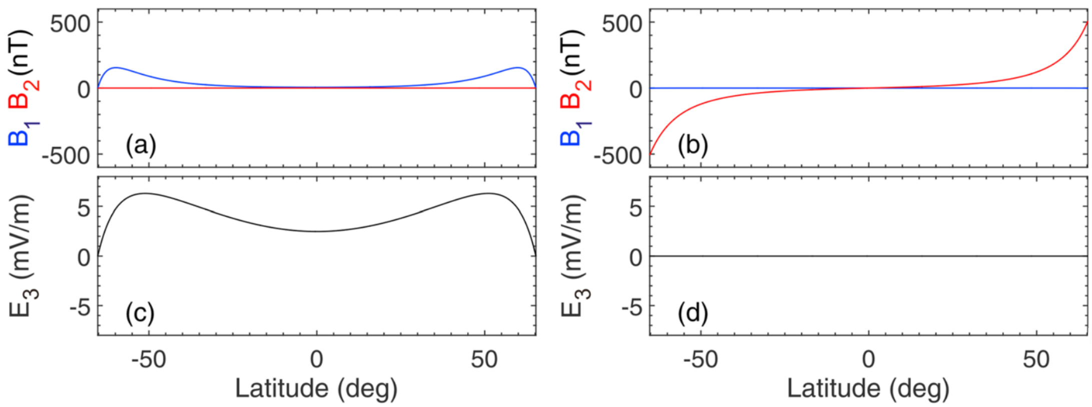

Figure 4.2: Figure 1 from C. Wang, Rankin, Y. Wang, et al. 2018. Eigenmode for a m =-35, 10mHz poloidal mode excited at L = 5.7. B_1 is referring to the compressional field component, not the total magnetic field. The fields in the right column are taken a quarter of a wave period after those on the left. The compressional magnetic field (top left panel in blue) and azimuthal electric field (bottom left panel in black) are in phase. The radial magnetic field (top right panel in red) is 90 degrees out of phase with the other two components.

The primary difference between the models is the difference in phase between the three field components. The results from C. Wang, Rankin, Y. Wang, et al. 2018 show the B_1 and E_3 component in phase while the B_2 component is a quarter period out of phase. Our results have B_1 and B_2 in phase while the E_3 component is a quarter period out of phase. In order to check the correct phase between these components, we return to the definitions of the fields and Faraday's Law.

Since both methods are based on Rankin, Samson, and Frycz 1993 we look at the time-varying terms found there. A quarter period phase difference between these terms is due to a difference in the trigonometric term that describes the variation of the field in time. Here the magnetic field components are defined in terms of $\cos \omega t$ while the electric field is defined in terms of $\sin \omega t$. This definition leads us to believe that the two magnetic fields should be in phase and the electric field should be out of phase by a quarter wave period.

In order to compare the fields using Faraday's Law we begin be restating the poloidal mode approximation used at the beginning of our derivation. This leaves us with a background field-aligned magnetic field B_{11}, radial magnetic field B_2, and an azimuthal electric field E_3. Using Faraday's Law in dipole coordinates gives us

$$\frac{1}{h_1 h_2 h_3} \frac{\partial h_3 E_3}{\partial x_2} = -\frac{\partial B_{11}}{\partial t} \tag{4.46}$$

which requires that E_3 and B_{11} are out of phase with each other. This proves that the fields shown in Figure 4.2 are not physical and cannot correctly model ULF waves. Our fields do satisfy this initial validation using Faraday's Law.

The violation of Faraday's law by the field equations derived C. Wang, Rankin, Y. Wang, et al. 2018 is not obvious. The phase difference between the electric and magnetic field components is only required because of the poloidal mode assumption and the field components we are interested in. This means that there is no reason to assume that the fields would generally be out of phase. Looking at observational results will not show this phase difference preventing a verification through comparison. In order to find this error, we re-derived his field equations from the MHD equations outlined in Section 3.1.1.

Despite this error in Figure 4.2 we believe that the single particles dynamics presented in C. Wang, Rankin, Y. Wang, et al. 2018 is accurate but not correct due to improper fields. The model displays characteristics which appear to be consistent with observations (Kazue Takahashi et al. 2018; L. Li et al. 2018) but is quantitatively inaccurate due to the errors in the calculations of the fields.

4.3 Errors in Poloidal Mode Modeling

This settles the phase disagreement of the compressional magnetic field but the magnitude of the field in both results is also troubling. There are two reasons for this. The first is in both models the compressional magnetic field grow linearly with time, leading to large B_1 components that are not limited by any physical field component. Instead, both models use the artificial driver R_D to limit this component following the growth phase; which limits the validity of the model.

The second, and more important reason, is tied to the removal of the toroidal field components, E_2 and B_3. If we look at Faraday's Law in dipole coordinated, Equation 4.47, we see that there is a balance between the variations of E_2 and E_3 that limits the growth of the compressional magnetic field.

$$\frac{1}{h_1 h_2 h_3}\left(\frac{\partial h_3 E_3}{\partial x_2} - \frac{\partial h_2 E_2}{\partial x_3}\right) = -\frac{\partial B_{11}}{\partial t} \tag{4.47}$$

Since both models have assumed that $E_2 = 0$, any radially narrowing E_3 component will result in a growing B_{11} field. For waves of constant width this may be an appropriate assumption but both models simulate the narrowing of the wave using sinc $\frac{\Delta\omega t}{2}$. This narrowing is time dependent, meaning that the radial width of the fields decreases over time leading to larger variations in the B_{11} component over time. This effect is evident in both Figures 4.2 and 4.1. After three wave periods, B_{11} can as high as half of the earth's background magnetic field at the equator. This limits the application of both models to the point of irrelevance. Any attempt to model this kind of behavior must include a toroidal, $E_2 \neq 0$, in order to limit this growth.

In nature, this growth is limited by the toroidal mode which acts as an initial sink for the energy in the wave. This explains why the growth of the toroidal mode components occurs after the poloidal mode component and can be seen in the modeling done in Degeling et al. 2019. Future attempts to isolate the poloidal mode should include some threshold for the compressional magnetic field in order to artificially limit the strength of the field. However, I recommend that this be avoided entirely by modeling both field components or focusing on the toroidal rather than the poloidal mode.

4.4 Summary

We derived an analytic solution for the poloidal mode of a ULF wave. Comparisons were made with the results found in C. Wang, Rankin, Y. Wang, et al. 2018 which showed that their fields violated Faraday's Law and cannot be accurate. However, based on the particle trajectories and comparisons with observations shown later in the paper, the model still displays characteristics which are consistent with observations, but is not accurate because the fields do not satisfy Faraday's

Law. Regardless of this phase difference between the fields, the magnitude of the compressional magnetic field is unrealistic. This large magnetic field is a result of isolating the poloidal mode which prevents the development of an azimuthal magnetic field that could act as a sink. Future work should include both the toroidal and poloidal mode components. Additionally, by deriving the field components starting from their potentials, the concern regarding the satisfaction of Faraday's Law can be entirely avoided. One example of these kinds of fields can be found in Degeling et al. 2019.

Chapter 5

Test Particle Models

We have previously compared simulated ULF wave fields with other models in the literature. However, by studying the trajectories of particles interacting with these waves, the accuracy of fields can also be tested. These test particle simulations offer an additional perspective on the source of inaccuracies in the fields we model. Here we will outline the framework of our model and demonstrate the bench marking used to verify it. We highlight the impact of radial limiting of the wave on conserved quantities in both our fields and those reported in C. Wang, Rankin, and Zong 2015. This chapter concludes with a discussion of proper modeling assumptions that should be used going forward.

5.1 Particle Trajectory Modeling

We begin by defining the forces that will govern the motion of our particles. For a charged particle, its motion is completely governed by the Newton-Lorentz Force,

$$m\frac{d\mathbf{v}}{dt} = q(\mathbf{E} + \mathbf{v} \times \mathbf{B}) \tag{5.1}$$

where m is the mass of the particle, $\mathbf{v}$ is the the particles instantaneous velocity, $\mathbf{E}$ is the electric field and $\mathbf{B}$ is the magnetic field the particle experiences. For our simulations we will not be concerned with any relativistic effects as the ion velocities are much lower than the speed of light.

5.1.1 Runge-Kutta Integration

In order to compute the particle trajectories we used a fourth-order Runge-Kutta method to integrate Equation 5.1. This is possible because our equations of motion are ordinary differential equations. Each step in the integration process is defined by a constant, h, which is the step size or time step. The time-dependent general solution is expressed as,

$$y_{n+1} = y_n + \frac{1}{6}(k_1 + 2k_2 + 2k_3 + k_4) \tag{5.2}$$

$$t_{n+1} = t_n + h \tag{5.3}$$

The next position in the particle trajectory is y_{n+1} and is based off the current position y_n plus weighted values for different possible increments, k_n, with the greatest weight being given to increments at the midpoint, k_2 and k_3.

$$\begin{aligned} k_1 &= hf(t_n, y_n) \\ k_2 &= hf(t_n + \frac{h}{2}, y_n + h\frac{k_1}{2}) \\ k_3 &= hf(t_n + \frac{h}{2}, y_n + h\frac{k_2}{2}) \\ k_4 &= hf(t_n + h, y_n + k_3) \end{aligned} \tag{5.4}$$

The advantage of single-step integration methods is that they do not require any knowledge of the previous position of the particle, meaning that starting the integration does not require any special initialization, unlike a multi-step method.

Additionally, the Runge-Kutta method was used due to its ease in implementation. However, the two main limitations of this method are the increased computational time required for similar accuracy compared to multi-step methods and compound error that may result from each step taken, particularly for relativistic cases.

A fourth order Runge-Kutta method is used to integrate Equation 5.1 with respect to time and is represented in Cartesian coordinates as,

$$\begin{aligned}\frac{dv_x}{dt} &= \frac{q}{m}(E_x + v_y B_z - v_z B_y)\\ \frac{dv_y}{dt} &= \frac{q}{m}(E_y + v_z B_x - v_x B_z)\\ \frac{dv_z}{dt} &= \frac{q}{m}(E_z + v_x B_y - v_y B_x)\end{aligned} \tag{5.5}$$

However, our model requires us to be able to convert these Cartesian coordinate calculations into dipole coordinates, which are used in the calculations of the electric and magnetic fields. This is handled by the following equation,

$$\begin{bmatrix} F_x \\ F_y \\ F_z \end{bmatrix} = \begin{bmatrix} -\frac{2\cos\theta}{\delta}\frac{x}{r} - \frac{\sin\theta\cos\theta\cos\phi}{\delta} & -\frac{\sin\theta}{\delta}\frac{x}{r} + \frac{2\cos^2\theta\cos\phi}{\delta} & -\sin\phi \\ -\frac{2\cos\theta}{\delta}\frac{y}{r} - \frac{\sin\theta\cos\theta\sin\phi}{\delta} & -\frac{\sin\theta}{\delta}\frac{y}{r} + \frac{2\cos^2\theta\sin\phi}{\delta} & \cos\phi \\ -\frac{2\cos\theta}{\delta}\frac{z}{r} + \frac{\sin^2\theta}{\delta} & -\frac{\sin\theta}{\delta}\frac{z}{r} - \frac{2\cos\theta\sin\theta}{\delta} & 0 \end{bmatrix} \begin{bmatrix} F_1 \\ F_2 \\ F_3 \end{bmatrix}$$

where $F_{1,2,3}$ corresponds to a vector in dipole coordinates as described in Section 4.1.1 and $\delta = \sqrt{1 + 3\cos^2\theta}$.

The advantage of using this Newton-Lorentz method is that no approximation is needed in calculating the trajectory of a charged particle. The resolution of our simulations is limited only by our time integration step size, T_{step}. In our simulations we define our step size in fractions of a gyroperiod, T_{gyro}. Specifically, we use a hundredth of a gyroperiod, shown below,

$$T_{step} = \frac{1}{100} T_{gyro} = \frac{1}{100} \frac{2\pi m}{|qB|} \tag{5.6}$$

This method is efficient for simulating the trajectories of ions, which have a gyroperiod on the order of 0.01-1s in the inner magnetosphere. Electrons will have much shorter gyro-periods, as low as 10's of microseconds, due to the mass dependence on the period. Any attempt to model electron dynamics should use a guiding center model instead.

While improvements to computational time are always desired, for single-particle simulations the run times are relatively short, on the order of tens of seconds. Regarding relativistic cases, the ion energies we are currently focused on are far below any need for relativistic corrections and the simulation times are short. However, when dealing with electron calculations it may be necessary to switch to a multi-step integration method like a Boris integrator. Using a Boris integrator would improve the long term accuracy of these simulations which currently carry a 4th order error based on the time step used (Qin et al. 2013).

5.2 Benchmarking

5.2.1 Electric Fields

The first step in checking the validity of our particle integrator is to focus on the interaction of the particle with a constant electric field. Using Equation 5.1 we can compare the expected increase in particle energy and the distance the particle should travel with our simulated results over a given time period. We started with a test particle with no initial kinetic energy, an azimuthal electric field of 1mV/m, and no magnetic field . This particle was traced over 24 seconds giving an expected displacement of 4.49L, where L refers to L-shell, and an energy change of 28.6keV. Our simulated results differed by 0.04% with an analytic integrated solution and this error was not dependent on the step-sized used in our integration process.

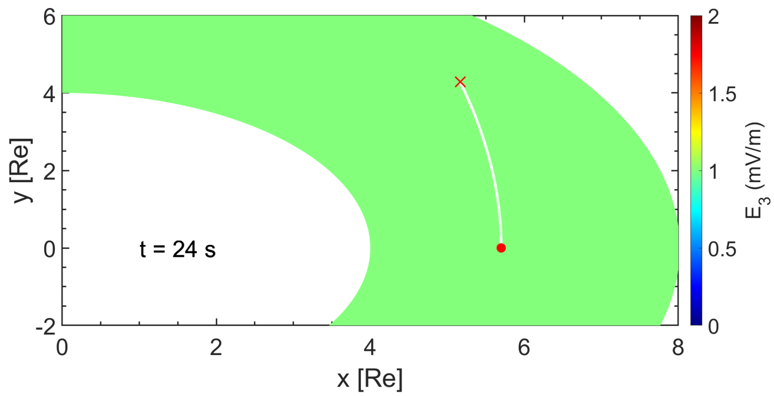

Figure 5.1: The motion of a hydrogen ion in a constant electric field set to 1mV/m. The particle dynamics are superimposed over the electric field. The red circle represents the particles starting location and the cross marks the particles current location. The particles trajectory is represented by the white line.

The trajectory of our test particle in an azimuthal electric field with constant amplitude can be seen in Figure 5.1. The image is a superposition of the particle trajectory over the simulated field. The particles motion trajectory is in white with a red circle representing the initial location and the red x representing the particles current location at the time denoted in the bottom left corner. The field is modeled in the azimuthal and radial direction with a Cartesian coordinate labeling. The field is modeled between a radial distance of 4-8L, creating the green band seen in Figure 5.1. This visualization is used throughout the remainder of the chapter.

Next, we used a simple time varying azimuthal electric field with the form, $E = cos(\omega t - m\phi)$. The simplest case is shown in figure 5.2 for a wave with m = -1 and a wave period of 100s. The negative sign in front of the wave number sets the direction of the wave propagation which is clockwise or westward propagating. The magnitude of the electric field strength is set at 0.1mV/m and is constant as

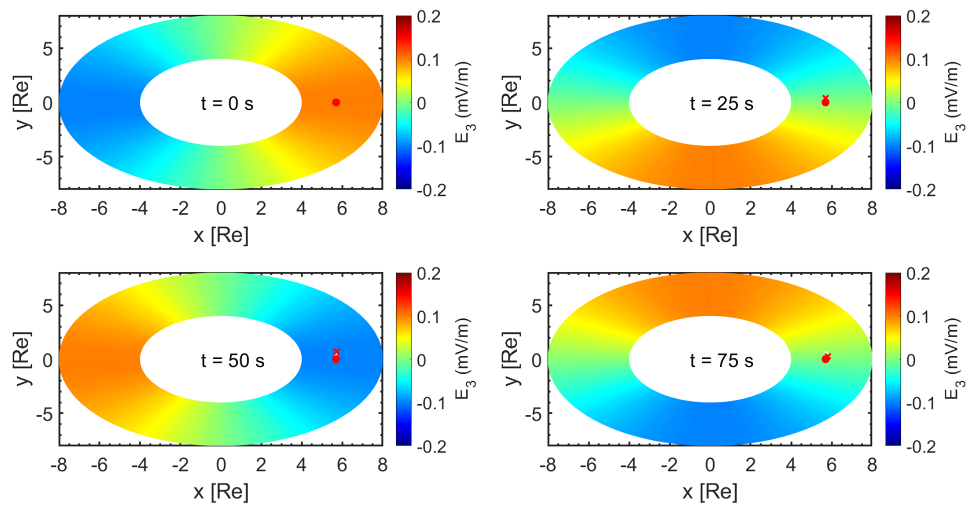

Figure 5.2: Variation in the azimuthal electric field with m = -1 and a wave period of 100s between L = 4 and L=8. Each panel is taken 25s after the previous, starting at 25s.The dot and cross in each panel represent the start and current location of the particle, respectively.

a function of radius. The color bar is set so that a positive and negative azimuthal electric field is represented by orange and blue, respectively. We have plotted the field using a 25s interval to highlight the motion of the wave in this simple case. By following the positive section of the wave, it clearly completes a full counterclockwise rotation in 100s. Additionally, it is clear that the strength of the field is not radially dependent.

The particle dynamics are more obvious in figure 5.3. Each panel is taken over 50s intervals, with a wave period of 100 seconds, highlighting the moments of maximum negative and positive field strength. As the particle is accelerated off of the y-axis the x component of the azimuthal electric field pushes the particle radially outward. This re-occurs as the particle moves in the negative y direction

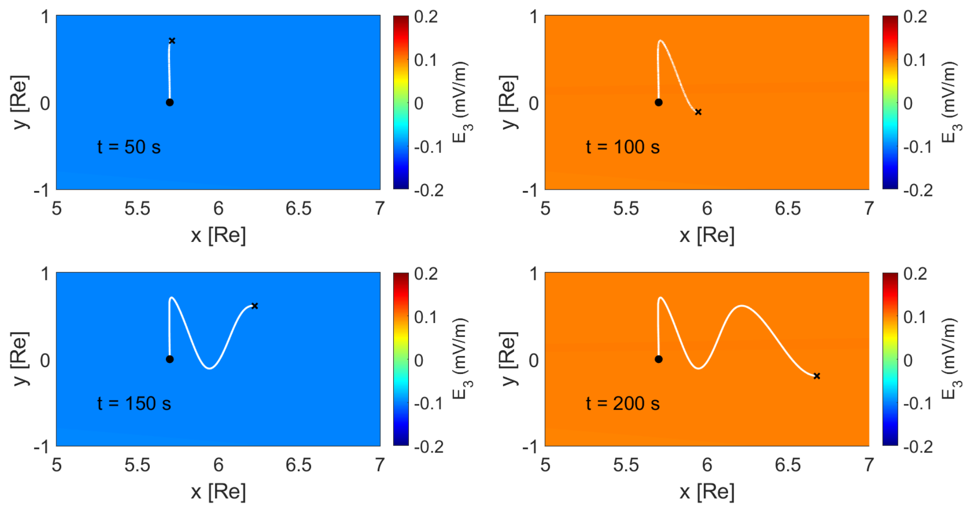

Figure 5.3: Variation in particle trajectory in an azimuthal electric field with m = -1 and a wave period of 100s between L = 4 and L=8. Each panel is taken 50s after the previous, between t = 50s and t = 200s. The dot and cross in each panel represent the start and current location of the particle, respectively.

since the particle has a negative velocity and is moving in a negative electric field. However, because the particle started in a positive field the net displacement is negative, as the particle velocity is greater during the second half of the wave period. Running the same electric field offset in phase by 50s yields a particle with an overall positive displacement for the same reason.

This analysis was repeated for the same electric field strength and period but m =-35 as shown in figure 5.4. The more drastic vertical drift of the particle is due to the larger wave number. As the particle accelerates in the positive field, it moves against the direction of propagation and quickly enters an area of negative electric field. The large wave number reduces the width of the individual wave fronts highlighting the asymmetric motion of the particle in the field.

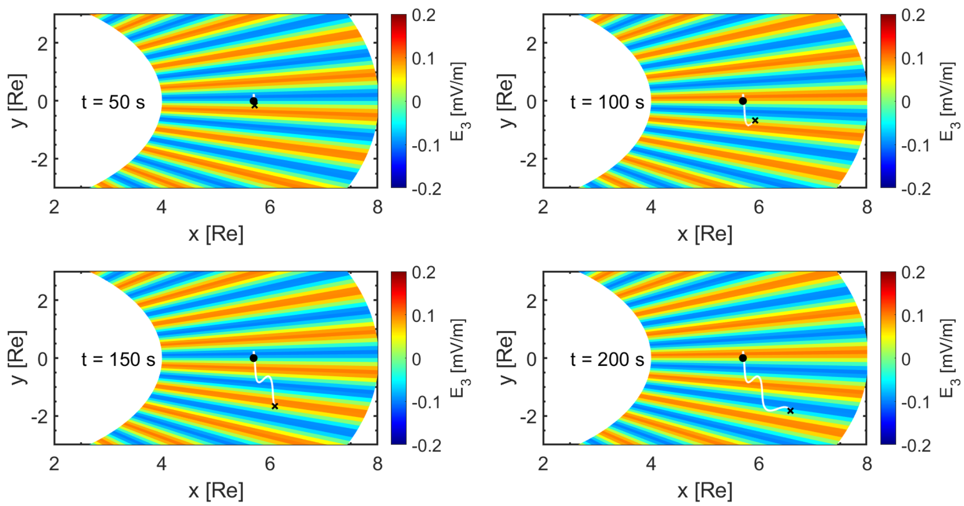

Figure 5.4: Variation in the particle trajectory in an azimuthal electric field with m = -35 and a wave period of 100s between L = 4 and L = 8. Each panel is taken 50 seconds after the previous, between t = 50s and t = 200s. The dot and cross in each panel represent the start and current location of the particle, respectively.

These tests ensure that the particle-wave interactions are consistent with the electric component of the Lorentz force equation. The test conducted with varying wave numbers also ensure that the wave period and wave number are correctly set in the model. The next step is to look at the magnetic component of the Newton-Lorentz force.

5.2.2 Magnetic Fields

The next series of tests focused on ensuring the magnetic field was accurately modeled, starting with a constant magnetic field and removing the electric field. We used a H^+ ion as our test particle to study the gyro-period and radius. We selected a 16nT field which has an expected gyro-period of 4.1s and a gyro-radius of $\Delta L = 0.52$. This test also confirmed that the mass of the test particle was correctly implemented as the gyro-radius is mass dependent. In figure 5.5 the particle follows the right hand rule and completes a gyro-orbit in just over 4s with a gyro-radius of approximately half an L-shell. All of these results show agreement with expected theoretical values.

This was followed by ensuring that the dipole magnetic field was correctly implemented based on the dipole field equation, 5.7.

$$B_{10}(L,\theta) = \frac{B_E}{L^3}\frac{(1+cos(\theta)^2)^{1/2}}{sin(\theta)^6} \tag{5.7}$$

where B_{10} is the Earth's background magnetic field as a function of L and θ, where theta is the co-latitude angle. B_E is the equatorial magnetic field at the Earth's surface, approximately 3.11×10^{-5}T. This thesis is only interested in the motion of particles in the equatorial plane and with 90 deg pitch angle, allowing us to simplify the definition of the background field to,

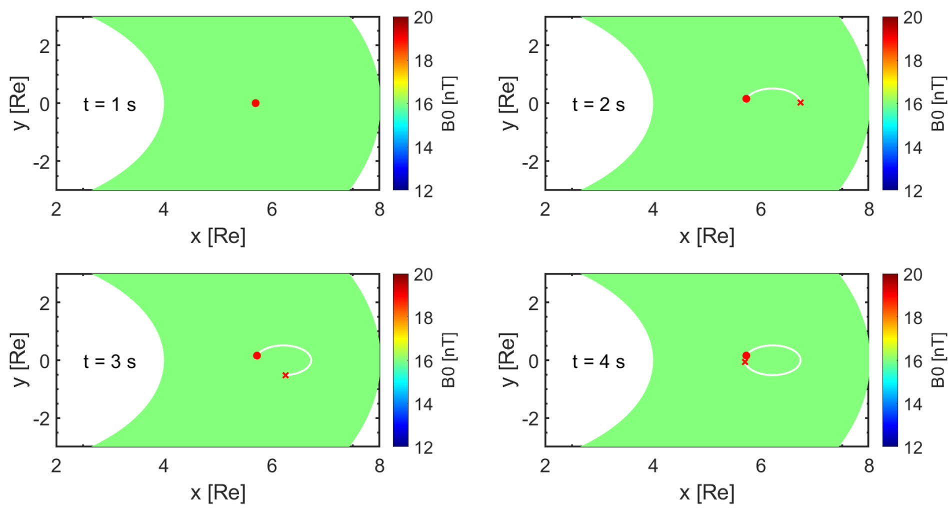

Figure 5.5: 133keV Hydrogen gyro-motion in a constant magnetic field of 16nT. The magnetic field is directed out of the page and the particle starts with an initial velocity in the positive y-direction. Panels range from 0s to 4s in intervals of 1s. The dot and cross in each panel represent the start and current location of the particle, respectively.

$$B_{10}(L) = \frac{B_E}{L^3} \tag{5.8}$$

In order to confirm that the field was correctly implemented we first check the magnetic field at the released location of $L = 5.7$ which agrees with the calculated value of 167nT. We then compare the simulated drift period with the theoretical value. The theoretical value for a particle at $L = 5.7$ and an energy of 133keV is 3480s. Our simulated results agree with these values and also give us a chance to compare the gyro-period and gyro-radius in this new magnetic field which also agree. This motion is illustrated in figure 5.6.

The constant field tests confirmed that our particle's mass and the background magnetic field were correctly implemented in our model, while the dipole field ensured that our dipole model was accurate and that drift motion is accurately simulated.

5.3 Drift Resonance

Putting together the dipole field and the time varying electric field we can begin to simulate drift resonance. The resonance energy was calculated from the drift resonance equations outlined in Section 3.3. We expect to see the particle oscillate in the wave profile as it gains energy from the positive E_3 component of the wave. This energization results in an outward radial drift and an increase in azimuthal velocity which will put the particle out of phase with the positive field and eventually place it in a negative phase. Here, it will lose energy and slow down, drifting inward and entering a positive wave front.

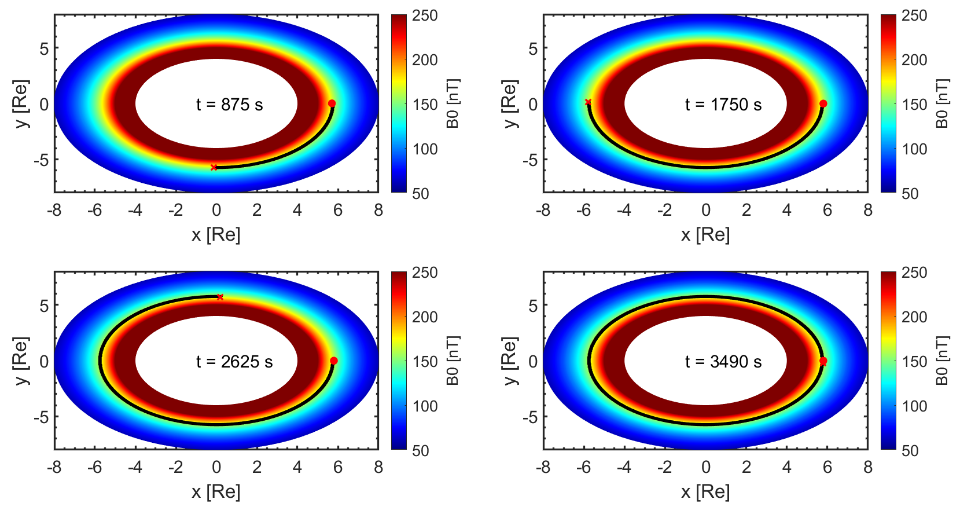

Figure 5.6: 133keV Hydrogen ion drift motion in a dipole magnetic field. Each panel is a snapshot over 875s intervals between t= 0s and t= 3490s. The calculated drift period is 3480s. The dot and cross in each panel represent the start and current location of the particle, respectively.

5.3.1 Simplified Fields

In order to test our model we define a simplified version of the poloidal mode fields. We start by defining the E_3 so that the curl of E_3 is zero in poloidal mode components. This is most easily accomplished by defining the components as,

$$\begin{aligned} E_3 &= E_0 \frac{L_{res}}{L} cos(\omega t - m\phi) \\ B_{11} &= \frac{E_0}{c} sin(\omega t - m\phi) \end{aligned} \tag{5.9}$$

These definitions ensure that Faraday's law is obeyed and the divergence of the magnetic fields is zero for all time. Additionally, it allows us to set the strength of the electric field at the resonance location from our initial parameters. For our test case we set a constant E_0 at 3mV/m, m = -35, a wave period of 100s, and a resonance location, L_{res}, at $L = 5.7$. Figure 5.7 shows the trajectory of a 133keV H^+ ion with a 90° pitch angle. The 133keV ion appears to satisfy the drift resonance condition and the motion of the particle agrees with the expectations stated above. During the first 250s of the simulation, the particle loses energy to the field and drifts outward. It then enters a positive wave front, visible at t=500s, where it gains energy and proceeds to drift inwards as seen at t=750s. The particle then enters an area of negative electric field and begins to drift outward again, t = 1000s. Due to the large width of the fields and the constant field strength, the particle will repeat this cycle for the remainder of the simulated time.

In order to further study the dynamics of the particle and ensure that the drift resonance condition is truly satisfied we turn to Figure 5.8. The first plot shows the change in the particle's radial position with the width of the line corresponding to the gyro-motion of the particle. The next two plots are the change in energy and magnetic field which vary out of phase with the first plot as expected. The variation in the change of energy is small over a gyroperiod which is why the width of the energy plot is thinner than the other two. Both differences are calculated by

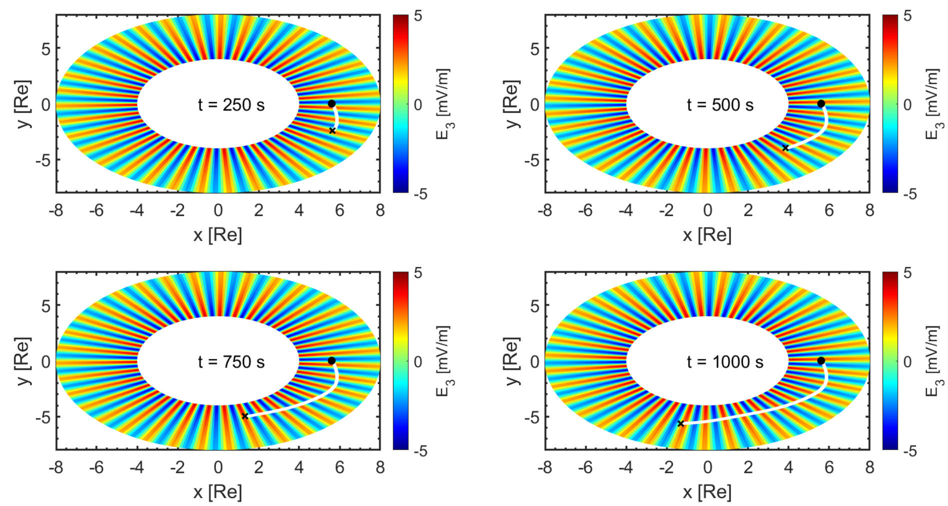

Figure 5.7: Variation in 133keV hydrogen ion drift motion in a radial azimuthal electric field with m = -35 and a wave period of 100s between L = 4 and L=8. Each panel is taken 250s after the previous, between t = 250s and t = 1000s. The dot and cross in each panel represent the start and current location of the particle, respectively.

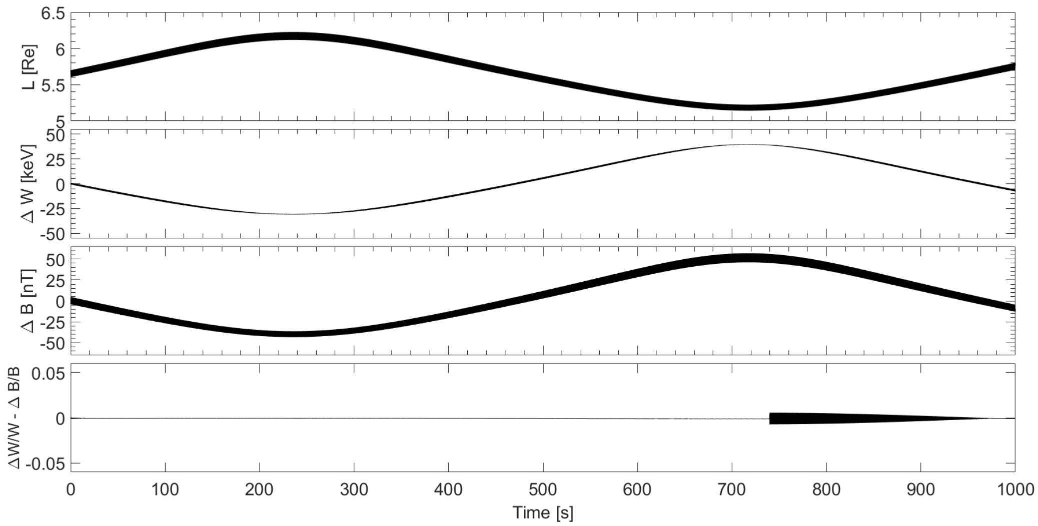

Figure 5.8: From top to bottom, the radial position, change in particle energy, change in magnetic field experienced by the particle, and change in conserved quantity for a 133 keV hydrogen ion as a function of time. All wave parameters are the same as those in figure 5.7.

finding the difference between the current value and the initial value at $t = 0$. The variations in energy and radial position all agree with the equatorial plot shown in Figure 5.7.

The final plot shows the differences between the normalized magnetic field and energy. This is an alternate form of the first invariant, μ, which is normally used to verify if motion is adiabatic. The reason that the magnetic moment is not used is because the first invariant is calculated from the gyro-center of the particles motion. The stand in used is derived form the definition of μ and assumes that the variation in the first invariant is small when compared to the variations in the magnetic field. This means that as long as variations in the magnetic field are small over the time and length scales associated with the particles gyromotion,

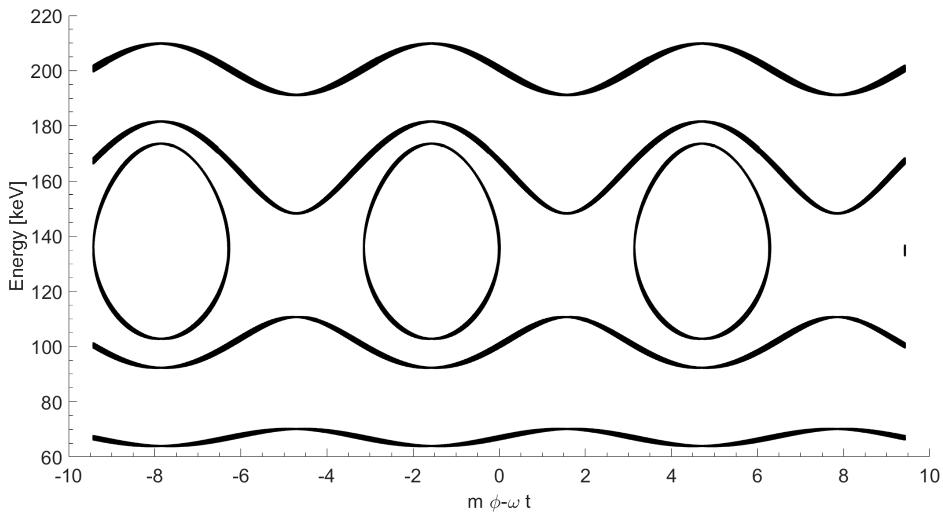

Figure 5.9: Poincaré plot of 5 hydrogen ions of various energies in the wave frame with identical magnetic moments. The y-axis spans three consecutive wave fronts. Particle energies span half to one and a half times the resonance energy in steps of a quarter of the wave's resonance energy. Here the resonance energy is set at 133keV. The resonant energy ion is the only one to form closed islands. All wave parameters are the same as those in Figure 5.7.

our conserved quantity should be invariant.

This quantity should be centered around zero with the variations resulting from the gyro-variations in the magnetic field. However, we used an average over the gyro-period in order to eliminate this variation. This results in the variation seen at t=750s which is a byproduct of this averaging but is not related to the physical behavior of the particle. This error is visible in Figure 5.10 as well. The error is a result of averaging over the gyroradius which becomes offset at t=750s and leads to a large variation in the energy of the particle that is not physical.

Figure 5.9 shows a Poincaré map for 5 hydrogen ions with energies from half to one and a half times the resonance energy in steps of a quarter of the waves resonance energy. The energies are plotted in the wave frame with the same parameters as defined in Figure 5.7. The resonant energy particle executes closed orbits which illustrates that they are trapped between wave fronts. This proves that 133keV energy is in fact the resonance particle energy for this specific wave. Additionally, we can see that the total energy variation of the resonant particle is limited between 105-170keV. This corresponds to a variation of around 40keV which agrees with the second panel in figure 5.8. The higher and lower energy particles move between wave fronts which are represented by their movement across the three wave fronts depicted.

In order to better understand the importance of preserving Faraday's law we will look at a specific case where it is violated. We will use the same fields defined in equation 5.9 but we will remove the radial dependency in E_3.

$$\begin{aligned} E_3 &= E_0 cos(\omega t - m\phi) \\ B_{11} &= \frac{E_0}{c} sin(\omega t - m\phi) \end{aligned} \tag{5.10}$$

This specific definition is used for a variety of reasons. First, while Faraday's law is violated these equations maintain the divergence of the magnetic fields being zero. Second, while these equations no longer satisfy Faraday's law in a dipolar coordinate system, they do satisfy Faraday's Law in spherical coordinate system, making it a simple mistake to make. Finally, the similarities between Equations 5.9 and 5.10 allow for a direct comparison that can highlight the errors in particle trajectories that result from violations of Faraday's law.

As above, for our test case we set a constant E_3 at 3mV/m, m = -35, a wave period of 100s, and $L_{res} = 5.7L$. Figure 5.10 shows the particle trajectory parameters for a 133keV H^+ ion with a 90° pitch angle. The first three panels

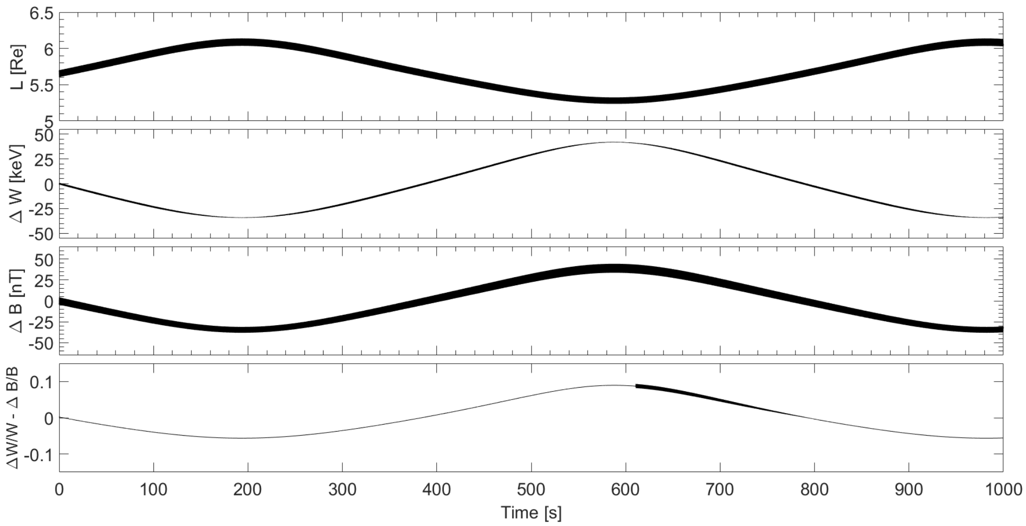

Figure 5.10: From top to bottom, the radial position, change in particle energy, change in magnetic field experienced by the particle, and change in conserved quantity for av133 keV hydrogen ion as a function of time. The parameters of the wave are: m =-35, L_{res} = 5.7Re, and a wave period is 100s. E_3 is constant across all L-shells.

show similar variation to those found in the corresponding panels in Figure 5.8. However, the fourth panel shows that our conserved quantity is no longer constant. This variation scales with the electric field strength and is a direct result of the violation of Faraday's law.

Figure 5.11 shows the Poincaré plot corresponding to this particle trajectory. The closed islands still form at the resonant energy but the variations in the off-resonant trajectories have a more drastic asymmetry when compared with Figure 5.9. This is most likely due to the radial variation of h_3E_3 in our new field definition. This test case shows that a resonant particle does not necessarily conserve the first adiabatic invariant if the fields do not satisfy Faraday's law. This allows

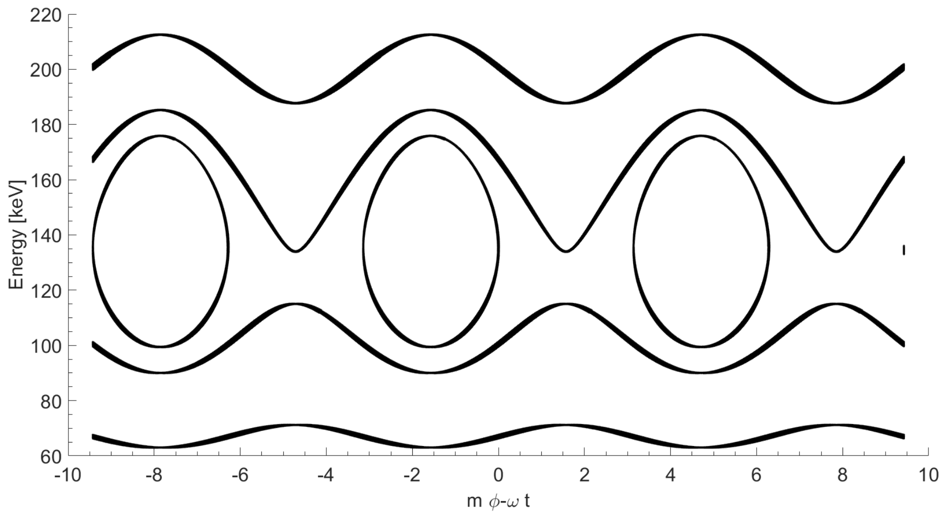

Figure 5.11: Poincaré plot of 5 hydrogen ions of various energies in the wave frame with identical magnetic moments. The y-axis spans three consecutive wave fronts. Particle energies span half to one and a half times the resonance energy in steps of a quarter of the wave's resonance energy. Here the resonance energy is set at 133keV. All wave parameters are the same as those in Figure 5.10.

us to better understand why test particle simulations that seem to have reasonable trajectory parameters could have large variations in their conserved quantities.

5.3.2 Simplified Fields with Radial Limiting

Another area of interest is the impact of radially limiting poloidal mode field on the behavior of charged particles. The radial limiting effect is related to the cut-off scale associated with phase mixing of the ULF wave. We once again return to Equation 5.9 but this time we introduce a sinc function in order to limit the radial width of the wave, resulting in the following equations,

$$
\begin{aligned}
E_3 &= E_0 cos\frac{L_{res}}{L}(\omega t - m\phi)\,\mathrm{sinc}(\frac{\Delta\omega t}{2}) \\
B_{11} &= \frac{E_0}{c} sin(\omega t - m\phi)\,\mathrm{sinc}(\frac{\Delta\omega t}{2})
\end{aligned}
\tag{5.11}
$$

The sinc function is used in order to more directly compare with the fields discussed in Section 4.1.6 and those used in C. Wang, Rankin, and Zong 2015.

Two different cases were used in order to better understand this radial variation. The first is time-independent, with time, t, set to a constant value, T= 100s. The radial variation of the wave is held constant, with the sinc function portion defined as, sinc($\frac{\Delta\omega T}{2}$. The second case is time-dependent and places no restrictions on the time component of the sinc function. These two cases correspond to a wave with radial width fixed at around 3Re and a narrowing field width. We will use the same parameters as in the previous cases: we set a constant E_0 at 3mV/m, m = -35, a wave period of 100s, and L_{res} = 5.7. Figure 5.12 shows the particle trajectory parameters for a 133keV H^+ ion with a 90° pitch angle. The left panels are for the time-independent case and the right panel shows the time-dependent case. Both cases are shown at t = 500s and t = 1500s during the simulation.

As previously discussed in Section 4.3, the introduction of radial limiting will result in an increasing background magnetic field. We expect that this increase in B_{11} will cause the variation in our conserved quantities to increase. This is due to the fact that our conserved quantity is defined in terms of the total magnetic field. The large radial gradients in the electric field lead to a large B_{11} component. In our assumption of our conserved quantity we have assumed that the variation in B_{11} would be small over all time and space. As B_{11} grows to a similar order of the background field the regions where the particle would normally be able to move with it's adiabatic invariant being constant are no longer physical. This breakdown of adiabatic behavior due to large B_{11} components will occur in both our conserved quantity and a guiding center μ calculation. Physically, the variation

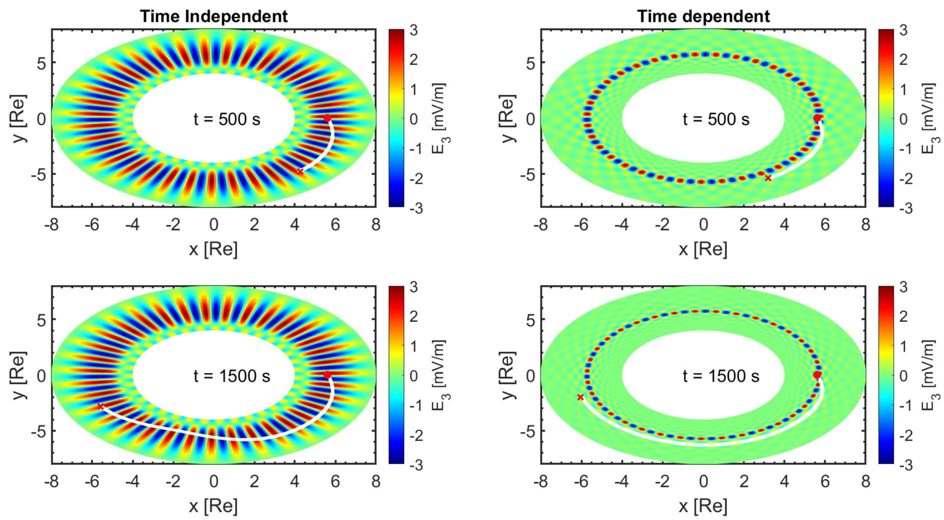

Figure 5.12: Drift resonance between a 133keV hydrogen ion and a radial azimuthal electric field with m = -35 and a wave period of 100s between L = 4 and L=8. The left column shows the trajectory in a wave front that has a fixed radial width that is not time-dependent.The right shows the trajectory in a wave front that has a radial width that decreases over time. The dot and cross in each panel represent the start and current location of the particle, respectively.

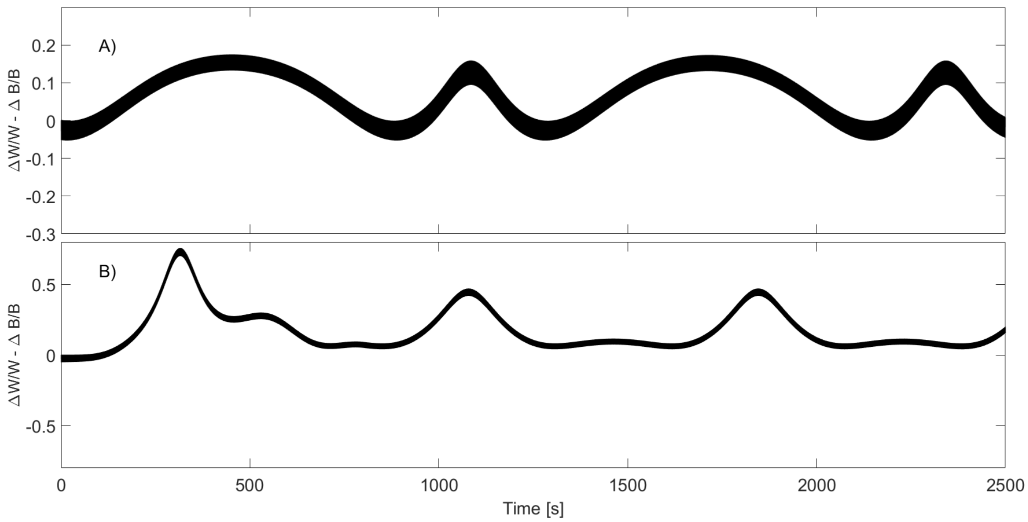

Figure 5.13: A comparison of the variation between the time independent, (A), and time dependent, (B), radial width cases shown in figure 5.12. The overall variation in the conserved increases as the radial width of the wave narrows.

of the fields over a gyroperiod will lead to non-uniform gyromotion. This means that the invariants can no longer be considered constant which is required for these quantities to be conserved.

Figure 5.13 shows the conserved quantity for both cases. The top panel, panel A, shows the variation for the t = 100s case and the bottom panel, panel B, shows the variation for the time dependent radial width case. As expected, we see that case A with less radial limiting results in smaller variations in the conserved quantity while case B shows larger variations.

5.4 Poloidal Mode Model Comparisons

5.4.1 Comparison with Published Models

Now that we have established a foundation for the validity of the particle integrator and have studied particle behavior using simplified fields we can move on to comparison with more complete poloidal mode field equations. We begin by looking at the fields defined in C. Wang, Rankin, and Zong 2015 and C. Wang, Rankin, Y. Wang, et al. 2018. Recall that these fields have been derived using a poloidal mode assumption that violates Faraday's law, which means that they should suffer from the same errors in the conservation of the first adiabatic invariant that we saw in figure 5.13.

However, there are two significant variations between this model and the simplified fields previously discussed. The first, and most important, is that the fields are not constant with respect to time. These fields are made up of a growth, constant, and a decay period. During the growth period, the fields grow linearly in strength with respect to time, and are implemented using an artificial driver, R_D. During the constant phase, this driver is turned off and the fields remain constant. Finally the waves experience an exponential decay during the decay phase.

Secondly, the radial dependency of the fields is far more complicated than the simplified 1/r variation discussed in equation 5.9. Figure 5.14 shows the particle parameters for a 133keV H^+ ion with a 90° pitch angle in a poloidal mode field. The 133keV satisfies the drift resonance condition for a wave with m = -35, L_{res} = 5.7Re, and the wave period is 100s. The wave fields grow linearly for 800s and then remain constant for 700s before it decays by 2500s.

The first panel shows a particle that drifts radially inward and outward with a far higher frequency than previously seen. Regardless, the variation in the particles

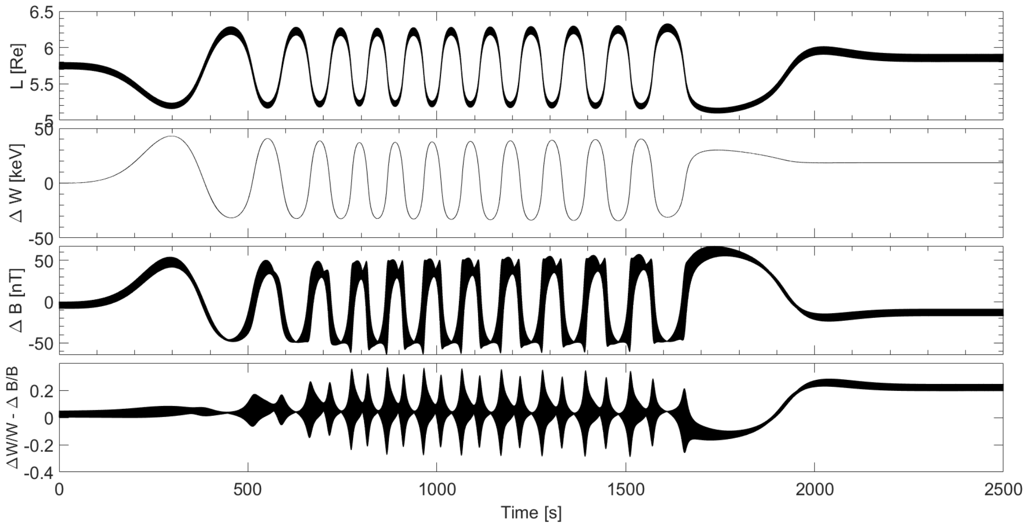

Figure 5.14: From top to bottom, the radial position, change in particle energy, change in magnetic field experience by the particle, and change in conserved quantity for 133 keV hydrogen ion as a function of time. The fields used are defined based on the work of C. Wang, Rankin, and Zong 2015. The parameters of the wave are: E_3 = 3mV/m, L_{res} = 5.7Re, and the wave period is 100s. The waves are set to grow for 800s, remain constant until t = 1500s, and then decay.

motion suggests that it is still resonating with the wave. The second plot agrees with the first, the maximums in energy correspond to minimums in radial position, as expected. Crucially, the shape of the first two panels perfectly match the results seen in figure 2, panel 1 of C. Wang, Rankin, Y. Wang, et al. 2018. Note that the variation in energy during the constant phase is similar to the results from the simplified model. The magnetic field agrees with the first panel but there are some sharper structures that seem to develop after t = 600s. The fourth panel shows a large variation in the conserved quantity that grows larger as the fields grow in strength. As expected, the variation in the conserved quantity or the magnetic moment, is similar in order of magnitude to those seen in Figure 5.13. There is also a non-zero change in the conserved quantity by the end of the simulation, T = 2500s. This suggests that the fields used in C. Wang, Rankin, Y. Wang, et al. 2018 and C. Wang, Rankin, and Zong 2015 suffer from the same growing B_{11}.

Figure 5.15 shows the Poincaré plots associated with the field previously discussed. Here the resonant energy islands are still closed and the off resonance trajectories are open but the resonance islands are sheared to the right. This means that the particles are not constrained to a single wave front and are in fact moving between three wave fronts rather one. For the center island, it reaches a minimum energy while in phase with the wave behind its initial launch and a maximum when it has accelerated into the wave front ahead of its initial position. It is unclear why this would be the case. However, the change in particle energy is limited between 100-150keV which agrees with both figure 5.14 and the results from the simplified model.

5.4.2 Chapter 4 fields

We now return to the fields defined in section 4.1.6 and study the resulting particle trajectories. The fields parameters are set as established in section 5.4.1. Figure

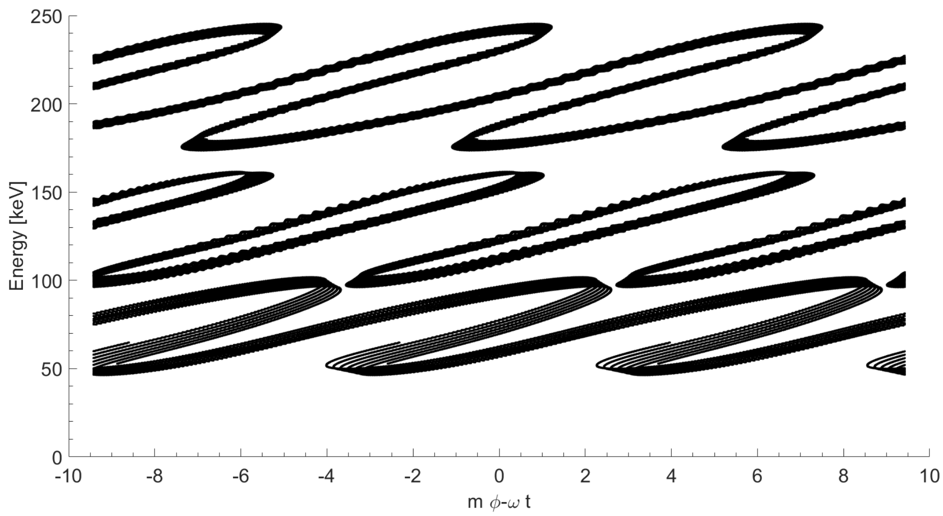

Figure 5.15: Poincaré plot of 133keV hydrogen ions in the wave frame. All wave parameters are the same as those in figure 5.14

5.16 shows the trajectory parameters as a function of time.

The first panel shows a particle that slowly begins to drift radially outward before oscillating around L = 6 while the gyro-radius increases to almost 1Re. The second panel shows an impossibly large increase in the particle energy up to a threshold value. The magnetic field agrees with the first panel as it decreases but continues to oscillate around a decrease of 25nT. The difference between the changes in energy and magnetic field would lead us to expect that our invariant will not be conserved which agrees with the fourth panel. Comparing the magnitude of the variation with the results previously discussed, it is clear that this error is far larger than we have seen resulting from radial limiting.

The exact cause of this large variation in our conserved quantity is not fully understood. One possible source could come from our assumption of leading order terms in Section 4.1.6. When we returned to those equations we found that some

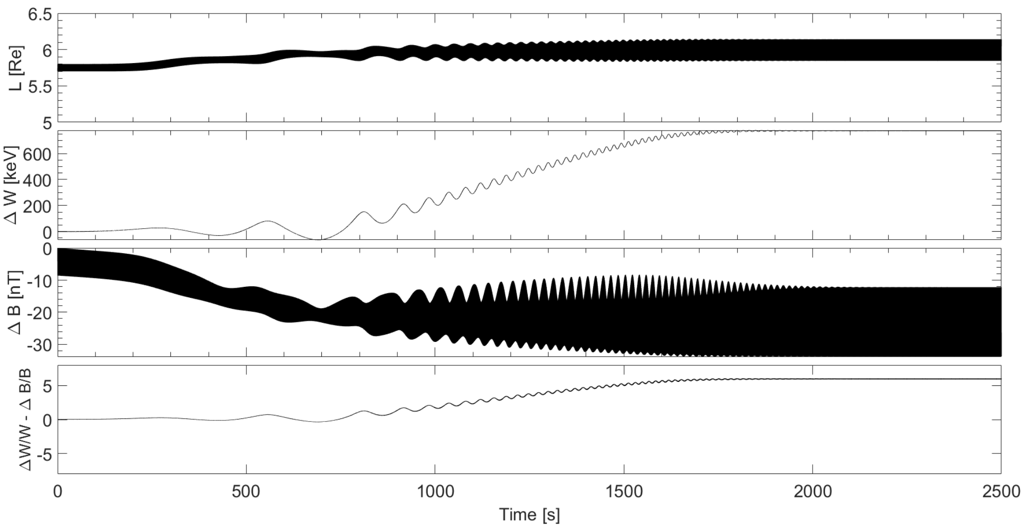

Figure 5.16: From top to bottom, the radial position, change in particle energy, change in magnetic field experienced by the particle, and change in conserved quantity for 133 keV hydrogen ion as a function of time. The fields used are defined in Section 4.1.6. The parameters of the wave are: m = -35, L_{res} = 5.7Re, and the wave period is 100s. The waves are set to grow for 800s, remain constant until t = 1500s, and then decay.

secondary terms that were assumed to be insignificant were of similar order to our leading terms. This means that our current field equations are missing a term that could have a significant impact on the variation on the B_{11} component. This uncertainty, combined with the large B_{11} strength that developed from the poloidal mode assumption could lead to large variations in our conserved quantity and, consequently, energy. However, this theory has not been tested and should be studied more closely.

The corresponding Poincaré plot, Figure 5.17, supports the theory that the particle is initially energized outward but quickly loses resonance with the wave and surfs the outer edge of the wave at higher energy. The particle begins with a nearly closed island in the wave frame but continues to gain energy and move ahead of the wave, represented by the progression of the particle to the right, over the first three wave periods. After that, its increase in energy brings it out of the wave frame where it is able to move between wave fronts, as if it were released with a non-resonant energy. The particle dynamics and the width of the initial islands are all consistent with figure 5.16.

5.5 Discussion

The fields derived in Section 4.1.6 and those used in C. Wang, Rankin, and Zong 2015 and C. Wang, Rankin, Y. Wang, et al. 2018 show variations in their conserved quantities that is not consistent with adiabatic drift resonance. These variations are also not consistent with observations of guided poloidal mode Alfvén waves. These observations show that while high-m waves do exist they have far smaller B_{11} components than those reported by both models. This small B_{11} is required in order to accurately model these high-m guided poloidal mode waves (Mann, Wright, and Hood 1997).

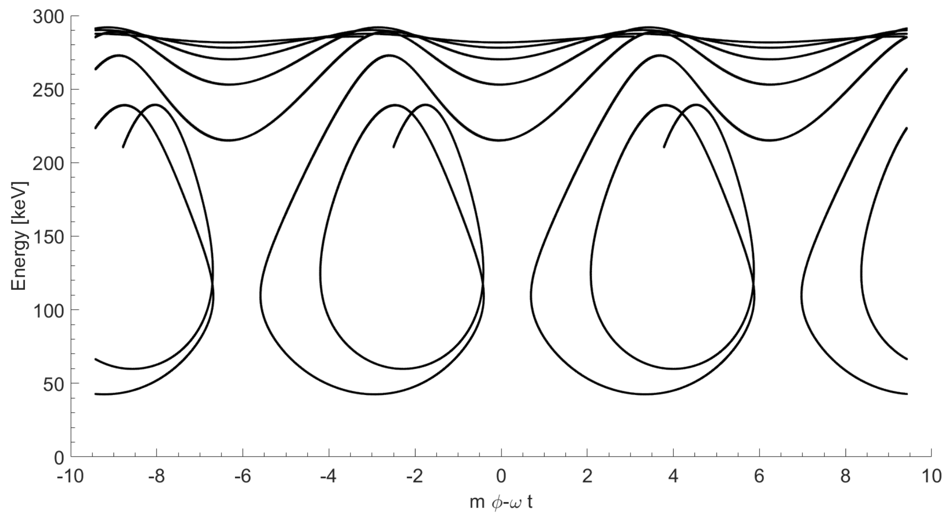

Figure 5.17: Poincaré plot of 133keV hydrogen ions in the wave frame. All wave parameters are the same as those in Figure 5.16

As previously discussed in Section 4.3, the large B_{11} fields are a result of the poloidal mode approximation. This assumption requires that the E_2 component that would balance the phase mixing that results from the $\frac{\partial h_3 E_3}{\partial x_2}$ portion of Faraday's law, Equation 4.47, is zero. C. Wang, Rankin, and Zong 2015 claim that they have limited the growth of the B_{11} component by limiting the driver term, R_D for a short period of time. However, there are several issues with this. First, even using the limited growth period they report, allows the B_{11} component to grow to over half of the Earth's background magnetic field at the equator. This means that even if limiting the time that the R_D was active was an appropriate method of modeling the system, the rate at which the field grows limits the validity of the model and leaves the model unsuitable for use.

The second is that the limiting of R_D is not sufficient to limit the growth of the B_{11} component to the growth period of the wave. This error is evident in both their fields and ours. We found that the B_{11} fields continued to grow over the constant and decay phase of the wave for both models. This means that even if the driver were only active for a short period of time, the growth of B_{11} is not limited by it. Again, the large compressional fields quickly becomes comparable to the Earth's magnetic field, which is unphysical and inconsistent with observations. The time at which this occurs varies based on the driver strength but for the case established in C. Wang, Rankin, and Zong 2015 it occurs after only a few wave periods.

Finally, the use of an artificial driver to limit the growth of B_{11} does not ensure that the fields satisfy Faraday's law. It only acts to limit the violation to some, hopefully small, value. Without introducing an E_2 component, the system of fields that is used in both C. Wang, Rankin, and Zong 2015 and Section 4.1.6 do not accurately model the physical system of guided poloidal mode Alfvén waves. In reality, the rotation of flux tubes by an E_2 component prevents the compression of the plasma and increase in B_{11}. Without introducing the toroidal field components any attempt to model particle dynamics risks using fields that violate Faraday's law. At best, the results from such models require validation from a secondary model that is know to satisfy Faraday's law.

5.6 Closing Remarks

Moving forward, we recommend that any attempt to model high-m Alfvén waves include the toroidal field components in order to ensure that Faraday's law is satisfied without the need for artificial restrictions. Additionally, B_{11} needs to remain small but finite in order to agree with observed results and prevent violations of linear assumptions.

One example of a successful model that can be used for this kind of testing has been outlined by Degeling et al. 2019. Their field components are derived from the potentials for each of the components which ensures that the resulting fields satisfy Faraday's law. Additionally, their model is well constructed for studying high-m wave dynamics and could easily be implemented in a similar full Lorentz particle integrator.

Finally, we recommend that all of the results found in C. Wang, Rankin, and Zong 2015 and C. Wang, Rankin, Y. Wang, et al. 2018 be verified using fields that are known to satisfy Faraday's law.

Chapter 6

Conclusion

Chapter 1 outlined the environment and large scale behavior that impacts observations and simulations of wave-particle interactions between the Earth and the Sun. The Sun and solar wind are the primary source of disturbances in the Earth's magnetic field and the generation of Alfvén waves. We highlighted the key regions of the Earth's magnetosphere to help situate the reader with the areas of interest. Geomagnetic storms and substorms are briefly discussed in an effort to explain the type of IMF geomagnetic interactions that can result in ULF waves. We ended this chapter with an overview of the goals of this thesis.

A review of the key aspects of particle and wave dynamics are discussed in chapters 2 and 3. We reviewed the three adiabatic invariants, the derivation of hot and cold MHD equations and drift resonance. This theoretical background was used to derive the field equations and model particle trajectories in the following chapters of the thesis.

Chapter 4 outlines the definition of poloidal mode field components for high-m Alfvén waves in the inner magnetosphere. The key assumptions of the model and their validity are discussed in depth in the second half of the chapter. The chapter concludes with a comparison to the results published in C. Wang, Rankin, and Zong 2015. The chapter concludes with a critique of the assumptions based on Faraday's law and evidence of violations in both sets of field equations.

An outline of the modeling method begins chapter 5. A series of benchmarks are discussed that are used to defend the validity of the charged particle numerical integrator. Simplified fields are used to highlight irregularities in the first invariant during drift resonance between high-m ULF Alfvén waves and H^+ ions. We studied the particle dynamics that result from drift resonance between H^+ and the fields derived in C. Wang, Rankin, and Zong 2015 and the fields derived in chapter 4 of this thesis. We end with a discussion of the errors in poloidal mode assumptions and possible solutions.

There are numerous studies that would benefit from the type of analysis discussed in chapter 5. However, any future work should begin with fields that are known to satisfy both Faraday's law and keep B_{11} limited to a reasonable, physical value. Following this verification, we suggest analyzing the behavior of drift-bounce ions for particle with a variety of pitch angles or non-linear drift resonance and comparing it with the results found in L. Li et al. 2018. One could also look into comparing the relative energization of hydrogen and oxygen ion as outlined in Oimatsu, Nosé, Teramoto, et al. 2018.

Bibliography

Akasofu, S.-I. (1974). "Discrete, continuous and diffuse auroras". In: *Planetary and Space Science* 22.12, pp. 1723–1726. ISSN: 0032-0633.

Alfvén, H. (1942). "Existence of electromagnetic-hydrodynamic waves". In: *Nature* 150.3805, pp. 405–406.

Allan, W. and F.B. Knox (1979). "The effect of finite ionosphere conductivities on axisymmetric toroidal Alfvén wave resonances". In: *Planetary and Space Science* 27.7, pp. 939–950. ISSN: 0032-0633.

Allan, W. and E.M. Poulter (May 1992). "ULF waves-their relationship to the structure of the Earth's magnetosphere". In: *Reports on Progress in Physics* 55.5, pp. 533–598.

Balfour, S. (1860). "On the Great Magnetic Disturbance of August 28 to September 7, 1859, as Recorded by Photography at the Kew Observatory. [Abstract]". In: *Proceedings of the Royal Society of London* 11, pp. 407–410. ISSN: 03701662.

Barth, J. L., C. S. Dyer, and E. G. Stassinopoulos (2003). "Space, atmospheric, and terrestrial radiation environments". In: *IEEE Transactions on Nuclear Science* 50.3, pp. 466–482. ISSN: 0018-9499.

Baumjohann, W and R.A Treumann (1997). *Basic Space Plasma Physics.* Impreial College Press.

Cheng, C.C., J. Chao, and T. Hsu (Aug. 1998). "Evidence of the coupling of a fast magnetospheric cavity mode to field line resonances". In: *Earth, Planets and Space* 5.8, pp. 683–697.

Claudepierre, S. G., S. R. Elkington, and M. Wiltberger (2008). "Solar wind driving of magnetospheric ULF waves: Pulsations driven by velocity shear at the magnetopause". In: *Journal of Geophysical Research: Space Physics* 113.A5.

Degeling, A. W. et al. (2019). "Alteration of Particle Drift Resonance Dynamics near Poloidal Mode Field Line Resonance Structures". In: *Journal of Geophysical Research: Space Physics.* to appear in.

Dungey, J. W. (Jan. 1961). "Interplanetary Magnetic Field and the Auroral Zones". In: *Phys. Rev. Lett.* 6 (2), pp. 47–48. DOI: 10.1103/PhysRevLett.6.47.

— (1965). "The length of the magnetospheric tail". In: *Journal of Geophysical Research (1896-1977)* 70.7, pp. 1753–1753. DOI: 10.1029/JZ070i007p01753.

Echer, E., W.D. Gonzalez, and B.T. Tsurutani (2011). "Statistical studies of geomagnetic storms with peak Dst50nT from 1957 to 2008". In: *Journal of Atmospheric and Solar-Terrestrial Physics* 73.11, pp. 1454–1459. ISSN: 1364-6826.

Fairfield, D. H. et al. (2000). "Geotail observations of the Kelvin-Helmholtz instability at the equatorial magnetotail boundary for parallel northward fields". In: *Journal of Geophysical Research: Space Physics* 105.A9, pp. 21159–21173.

Green, C.A. (1979). "Observations of Pg pulsations in the Northern Auroral zone and at lower latitude conjugate regions, Planetary and Space Science". In: pp. 63–77.

— (1985). “Giant pulsations in the plasmasphere”. In: *Planetary and Space Science* 33.10, pp. 1155–1168. ISSN: 0032-0633.

Hasegawa, H. et al. (Aug. 2004). “Transport of solar wind into Earth’s magnetosphere through rolled-up Kelvin–Helmholtz vortices”. In: *Nature*.

Hudson, M. et al. (Jan. 2004). “A study of Pc-5 ULF oscillations”. In: *Annales Geophysicae* 22.

Kivelson, M.G and F. Bagenal (June 2014). *Encyclopedia of the Solar System (Third Edition)*. Ed. by Tilman Spohn, Doris Breuer, and Torrence V. Johnson. Third Edition. Elsevier, pp. 137–157.

Kivelson, M.G and C.T. Russell (1995). *Introduction to Space Physics*. Press Syndicate of the University of Cambridge.

Li, L et al. (Sept. 2018). “Nonlinear Drift Resonance Between Charged Particles and Ultralow Frequency Waves: Theory and Observations”. In: *Geophysical Research Letters* 45.17, pp. 8773–8782. ISSN: 0094-8276. DOI: 10.1029/2018GL079038. URL: https://doi.org/10.1029/2018GL079038.

Mann, I., A. Wright, and A. Hood (1997). “Multiple-timescales analysis of ideal poloidal Alfvén waves”. In: *Journal of Geophysical Research: Space Physics* 102.A2, pp. 2381–2390. DOI: 10.1029/96JA03034.

Oimatsu, S., M. Nosé, K. Takahashi, et al. (2018). “Van Allen Probes Observations of Drift-Bounce Resonance and Energy Transfer Between Energetic Ring Current Protons and Poloidal Pc4 Wave”. In: *Journal of Geophysical Research: Space Physics* 123.5, pp. 3421–3435.

Oimatsu, S., M. Nosé, M. Teramoto, et al. (2018). “Drift-Bounce Resonance Between Pc5 Pulsations and Ions at Multiple Energies in the Nightside Magnetosphere: Arase and MMS Observations". In: *Geophysical Research Letters* 45.15, pp. 7277–7286.

Qin, H. et al. (Aug. 2013). "Why is Boris algorithm so good?" In: *Physics of Plasmas* 20. DOI: 10.1063/1.4818428.

Radoski, H. R. (1967). "A note on oscillating field lines". In: *Journal of Geophysical Research (1896-1977)* 72.1, pp. 418–419. DOI: 10.1029/JZ072i001p00418.

Rae, I. J. et al. (2005). "Evolution and characteristics of global Pc5 ULF waves during a high solar wind speed interval". In: *Journal of Geophysical Research: Space Physics* 110.A12.

Rankin, R. (2014). "Linear Shear Alfvén Waves". In: *Unpublished Notes*.

Rankin, R., J. C. Samson, and P. Frycz (1993). "Simulations of driven field line resonances in the Earth's magnetosphere". In: *Journal of Geophysical Research: Space Physics* 98.A12, pp. 21341–21352.

Regi, M. (Aug. 2016). "ULF power fluctuations in the solar-wind parameters and their relationship with the relativistic electron flux at the geosynchronous orbit". In: *Il Nuovo Cimento C*.

Roederer, J. G. (1970). *Dynamics of Geomagnetically trapped Radiation*. Springer-Verlag.

Southwood, D.J., J.W. Dungey, and R. J. Etherington (1969). "Bounce resonant interaction between pulsations and trapped particles". In: *Planetary and Space Science* 17.3, pp. 349–361. ISSN: 0032-0633.

Swisdak, M. (2006). *Notes on the Dipole Coordinate System*. arXiv: physics/0606044 [physics.space-ph].

Takahashi, Kazue et al. (2018). “Van Allen Probes Observation of a Fundamental Poloidal Standing Alfvén Wave Event Related to Giant Pulsations”. In: *Journal of Geophysical Research: Space Physics* 123.6, pp. 4574–4593. DOI: 10.1029/2017JA025139.

Thorne, R.M. et al. (2013). “Rapid local acceleration of relativistic radiation-belt electrons by magnetospheric chorus”. In: *Nature* 504.7480, pp. 411–414.

Van Allen, J. A., C. E. McIlwain, and G. H. Ludwig (1958). “Radiation observations with satellite”. In: *Journal of Geophysical Research* 64.3, pp. 271–286.

Walker, A.D.M. (2005). *Magnetohydrodynamic Waves in Geospace*. IOP Publishing.

Wang, C., R. Rankin, Y. Wang, et al. (2018). “Poloidal Mode Wave-Particle Interactions Inferred From Van Allen Probes and CARISMA Ground-Based Observations”. In: *Journal of Geophysical Research: Space Physics* 123.6, pp. 4652–4667.

Wang, C., R. Rankin, and Q. Zong (2015). “Fast damping of ultralow frequency waves excited by interplanetary shocks in the magnetosphere”. In: *Journal of Geophysical Research: Space Physics* 120.4, pp. 2438–2451.

Werner, H. (1980). *Artist’s Conception of the Heliospheric Current Sheet*. URL: http://wso.stanford.edu/gifs/HCS.html (visited on 08/03/2010).

Yang, B. et al. (Jan. 2011). “The role of ULF waves interacting with oxygen ions at the outer ring current during storm times”. In: *Journal of Geophysical Research* 116.A1.